

Spring 2000

# A hybrid finite element-finite difference method for thermal analysis in a double-layered thin film

Teng Zhu

Follow this and additional works at: <https://digitalcommons.latech.edu/dissertations>

 Part of the [Other Computer Sciences Commons](#), and the [Other Mechanical Engineering Commons](#)

---

## **INFORMATION TO USERS**

**This manuscript has been reproduced from the microfilm master. UMI films the text directly from the original or copy submitted. Thus, some thesis and dissertation copies are in typewriter face, while others may be from any type of computer printer.**

**The quality of this reproduction is dependent upon the quality of the copy submitted. Broken or indistinct print, colored or poor quality illustrations and photographs, print bleedthrough, substandard margins, and improper alignment can adversely affect reproduction.**

**In the unlikely event that the author did not send UMI a complete manuscript and there are missing pages, these will be noted. Also, if unauthorized copyright material had to be removed, a note will indicate the deletion.**

**Oversize materials (e.g., maps, drawings, charts) are reproduced by sectioning the original, beginning at the upper left-hand corner and continuing from left to right in equal sections with small overlaps.**

**Photographs included in the original manuscript have been reproduced xerographically in this copy. Higher quality 6" x 9" black and white photographic prints are available for any photographs or illustrations appearing in this copy for an additional charge. Contact UMI directly to order.**

**Bell & Howell Information and Learning  
300 North Zeeb Road, Ann Arbor, MI 48106-1346 USA**

**UMI<sup>®</sup>  
800-521-0600**



**A HYBRID FINITE ELEMENT-FINITE DIFFERENCE  
METHOD FOR THERMAL ANALYSIS IN A DOUBLE-  
LAYERED THIN FILM**

by

**Teng Zhu M.S.**

**A Dissertation Presented in Partial Fulfillment  
of the Requirements for the Degree  
Doctor of Philosophy**

**COLLEGE OF ENGINEERING AND SCIENCE  
LOUISIANA TECH UNIVERSITY**

**May 2000**

**UMI Number: 9964413**

**UMI<sup>®</sup>**

---

**UMI Microform 9964413**

**Copyright 2000 by Bell & Howell Information and Learning Company.**

**All rights reserved. This microform edition is protected against  
unauthorized copying under Title 17, United States Code.**

---

**Bell & Howell Information and Learning Company  
300 North Zeeb Road  
P.O. Box 1346  
Ann Arbor, MI 48106-1346**

LOUISIANA TECH UNIVERSITY

THE GRADUATE SCHOOL

May 9, 2000

Date

We hereby recommend that the dissertation prepared under our supervision  
by Teng Zhu

entitled A Hybrid Finite Element-Finite Difference Method for Thermal  
Analysis in a Double Layered Thin Film

be accepted in partial fulfillment of the requirements for the Degree of  
Doctor of Philosophy in Applied Computational Analysis and Modeling

Wei Zhong Du

Supervisor of Dissertation Research

Richard F. Greechie

Head of Department

Applied Computational Analysis & Modeling  
Department (ACAM)

Recommendation concurred in:

Wei Zhong Du

Richard L. Hill

Richard F. Greechie

[Signature]

Advisory Committee

Approved:

[Signature]

Director of Graduate Studies

Approved:

[Signature]

Director of the Graduate School

[Signature]  
Dean of the College

## **ABSTRACT**

Thin film technology is of vital importance in microtechnology applications. For instance, thin films of metals, of dielectrics such as  $\text{SiO}_2$ , or Si semiconductors are important components of microelectronic devices. The reduction of the device size to the microscale has the advantage of enhancing the switching speed of the device. The reduction, on the other hand, increases the rate of heat generation that leads to a high thermal load on the microdevice. Heat transfer at the microscale with an ultrafast pulsed-laser is also a very important process for thin films. Hence, studying the thermal behavior of thin films or of micro objects is essential for predicting the performance of a microelectronic device or for obtaining the microstructures. The objective of the research is to develop a numerical method for solving three-dimensional heat transport equations in a double-layered cylindrical thin film with microscale thickness. To this end, the three-dimensional heat transport equations are discretized using the finite element method for the x-y directions and the finite difference method for the z direction. Since the obtained scheme is implicit, a preconditioned Richardson iterative method is employed so that the systems of equations become only two block tri-diagonal linear systems with unknowns at the interface. Using a parallel Gaussian elimination procedure to solve these two block tri-diagonal linear systems, a domain decomposition algorithm for thermal analysis of a double-layered thin film is developed. The numerical procedure is employed to investigate the temperature rise and temperature distribution in a double-layered thin film

with a cylindrical gold layer being on top of a cylindrical chromium padding layer. Numerical results are in good agreement with those obtained in previous research. The numerical method can be readily applied to the heat transport problem, where the shape of the film can be arbitrary in the x-y direction and where the film has multilayers.

## TABLE OF CONTENTS

<b>ABSTRACT</b> .....	<b>iii</b>
<b>LIST OF TABLES</b> .....	<b>vii</b>
<b>LIST OF FIGURES</b> .....	<b>viii</b>
<b>NOMENCLATURE</b> .....	<b>x</b>
<b>ACKNOWLEDGMENTS</b> .....	<b>xii</b>
<b>CHAPTER 1 INTRODUCTION</b> .....	<b>1</b>
1.1 General Overview .....	1
1.2 Statement of Problem.....	3
1.3 Research Objective .....	4
1.4 Research Methodology .....	5
1.5 Outline of the Dissertation.....	5
<b>CHAPTER 2 BACKGROUND</b> .....	<b>7</b>
2.1 Phonon-Electron Interaction Model.....	9
2.2 Phonon Scattering Model.....	18
2.3 Phonon Radiative Transfer Model.....	20
2.4 Dual-Phase-Lag Model.....	26
2.5 Double-Layered Thin Films.....	33
2.6 Dai and Nassar's Work.....	36
<b>CHAPTER 3 MATHEMATICAL MODEL</b> .....	<b>42</b>
3.1 Governing Equations for Temperature Distribution.....	42
3.2 The Boundary Conditions .....	45
3.3 The Initial Conditions .....	46
3.4 The Governing Equations for Stresses and Strains.....	46
3.4.1 Physics Equations .....	46
3.4.2 Differential Equations.....	47
3.4.3 Geometry Equations.....	47
<b>CHAPTER 4 NUMERICAL METHOD</b> .....	<b>49</b>
4.1 Introduction to Finite-Element Method .....	50
4.2 The Finite Element-Finite Difference Scheme .....	52
4.3 Preconditioned Richardson Iteration.....	57
4.4 A Domain Decomposition Algorithm.....	60
<b>CHAPTER 5 NUMERICAL RESULTS</b> .....	<b>64</b>

<b>CHAPTER 6 CONCLUSION AND DISCUSSION.....</b>	<b>82</b>
<b>REFERENCES.....</b>	<b>84</b>

## LIST OF TABLES

TABLE	DESCRIPTION	PAGE
2.1	Phonon-electron coupling factor $G$ for some noble and transient metals.....	13
5.1	Properties of gold and chromium .....	68

## LIST OF FIGURES

FIGURE	DESCRIPTION	PAGE
2.1	Energy transport through phonon-phonon or phonon-electron collision .....	8
2.2	Phonon/electron interaction and scattering in a thin film .....	10
2.3	Transient reflectivity change at the front surface of gold films .....	16
2.4	Transient reflectivity change at the rear surface of gold films.....	16
2.5	Phonon intensity $I_{\omega}$ and the azimuthal angle $\theta$ and $\phi$ defining the velocity.....	22
2.6	Temperature profiles in 1-D solid predicted by three different models.....	24
2.7	Temperature profiles in 1-D solid predicted by three different models.....	26
2.8	Comparison of the normalized autocorrelation of the laser pulse and others .....	29
2.9	Experimental results of reflectivity change.....	31
2.10	Normalized temperature change in gold film predicted by the dual-lag model ...	33
2.11	A padding layer made of different material placed behind the surface layer .....	34
2.12	3-D configuration of a double-layered thin film.....	34
2.13	3-D configuration of double-layered thin film with a rectangular shape.....	38
2.14	Temperature profiles along the vertical line .....	39
2.15	Temperature change on the surface of the gold layer.....	40
3.1	Configuration of 3-D double-layered thin film.....	44
4.1	A triangular element.....	52
4.2	The finite element mesh in the x-y cross-section .....	53
4.3	The staggered grids in the z direction for the double-layered thin film.....	55

5.1	3-D configuration of a double-layered cylindrical thin film.....	69
5.2	The finite element mesh in the x-y cross-section.....	70
5.3	Temperature profiles along the z direction .....	71
5.4	Temperature change on the surface of the gold layer .....	72
5.5	Contours of the temperature distribution in the x-z direction (t=0.2ps) .....	73
5.6	Contours of the temperature distribution in the x-z direction (t=0.25ps) .....	74
5.7	Contours of the temperature distribution in the x-z direction (t=0.5ps) .....	75
5.8	Cylindrical double-layered thin film.....	76
5.9	Temperature profiles along z direction with heat source at center area.....	77
5.10	Temperature change on the center of the surface of the gold layer .....	78
5.11	Contours of the temperature distribution in the x-z direction (t=0.2ps) .....	79
5.12	Contours of the temperature distribution in the x-z direction (t=0.25ps) .....	80
5.13	Contours of the temperature distribution in the x-z direction (t=0.5ps) .....	81

## NOMENCLATURE

$k$	thermal conductivity
$C_p$	specific heat
$M, K$	capacitance matrix and conductance matrix, respectively
$D_M, D_K$	diagonal matrices related to $M$ and $K$
$N, N_z$	the numbers of grid points
$Q$	heat source
$\bar{q} = (q_1, q_2, q_3)$	heat flux
$T, T^0$	temperature
$t$	time
$x, y, z$	Cartesian coordinates
$\Delta t, \Delta x, \Delta y, \Delta z$	time increment and grid sizes, respectively
$\omega$	relaxation parameter
$\varphi_p$	basis function
$\rho$	mass density
$\tau_q$	time lag of heat flux
$\tau_T$	time lag of temperature gradient
$C$	volumetric heat capacity
$G$	phonon-electron coupling factor

***Superscript***

$l = 1, 2$                     **layer 1 and layer 2**

$n$                                 **time step**

$i$                                 **iteration number**

***Subscript***

$p, m$                          **grid point indices**

$e, l$                             **electron and lattice, respectively**

## **ACKNOWLEDGMENTS**

I would like to express my gratitude and sincere appreciation to Dr. Weizhong Dai for his guidance through my research. He has been very supportive in every stage of my research work. So many meetings and discussion notes will never be forgotten. I thank him for his effort in helping me not only in academic, but also in personal aspects that motivates me to accelerate the completion of this dissertation.

I would also like to take the opportunity to thank Dr. Dick Greechie, Dr. Richard Gibbs, and Dr. Ben Choi for their guidance in this dissertation and for their support and service on my advisory committee. I wish to thank Mrs. Frances Welch at the College of Engineering and Science for her kindness and assistance.

I would like to say “ Thank you all. Your kindness makes me feel home being at Louisiana Tech University.”

Many thanks go to my friend Dr. Yukong Zhang. I thank him for taking time to discuss with me and to provide very useful thoughts regarding my research.

Finally, I dedicate this dissertation to my family. Their love and encouragement are always kept in my heart!

# **CHAPTER 1**

## **INTRODUCTION**

### **1.1. General Overview**

The first evaporated thin films were probably the deposits which Faraday obtained in 1857 when he exploded metal wires in an inert atmosphere. Further experimentation in the nineteenth century was stimulated by interest in the optical phenomena associated with thin layers of materials and by investigations of the kinetics and diffusion of gases. The possibility of depositing thin metal films in a vacuum by Joule heating of platinum wires was discovered in 1887 by Nahrwold and a year later adapted by Kundt for the purpose of measuring refractive indices of metal films. In the following decades, evaporated thin films remained in the domain of academic interest until the development of vacuum equipment had progressed far enough to permit large-scale applications and control of film properties. Thin film technology has grown rapidly in the last two decades and plays a key role in many segments of industry today. The industrial usage in antireflection coatings, front-surface mirrors, interference filters, sunglasses, decorative coatings on plastics and textiles, and the manufacture of cathode-ray tubes and electronic circuits has been very common. The reduction of the device size to microscale is of great interest, both in commercial applications and in scientific inquiry, because it has the advantage of enhancing the features of the device. For instance, thin films of metals or dielectrics, such as  $\text{SiO}_2$  or Si semiconductors, are important components of microelectronic devices. The

switching speed will be much faster under microscale. The size reduction, however, increases the rate of heat generation that leads to a high thermal load on the microdevice. Heat transfer at the microscale is also important for the processing of materials with a pulsed-laser. Examples in metal processing are laser micro-machining or deposition, laser patterning, laser processing of diamond films from carbon ion implanted copper substrates, and laser surface hardening. All of the above are associated with heating in thermal processing problems. When a significant temperature increase occurs in a solid, deformation occurs as a result of thermal expansion. Depending on how the solid is constrained, such a thermally induced deformation may either elongate, warp, bend the surface or develop a highly elevated stress within the solid if deformation is prevented. Deformation and stress waves are major causes of thermal damage in laser processing of materials. Hence, studying the thermal behaviors of thin films or of micro objects is essential for predicting the performance of a microelectronic device or for obtaining the desired microstructure. Further, the double-layered thin film problems are often encountered in micromanufacturing, such as a photoresist on a substrate in lithography or a gold surface layer on a chromium padding layer in laser processes.

Thermoelastic phenomena are of particular interest because they determine the quality of a device. Minimizing the deformation of the thin film is desired in all fields of micromanufacturing. Heat transport through thin films is of vital importance in microtechnology applications because temperature distribution is interrelated with stress and strain.

## 1.2. Statement of Problem

In the classical theory of diffusion, the heat transport for macroscopic models satisfies the Fourier's law:

$$\bar{q}(x, y, z, t) = -k\nabla T(x, y, z, t) \quad (1.1)$$

where  $\bar{q} = (q_1, q_2, q_3)$  is heat flux,  $T$  is temperature,  $k$  is coefficient of conductivity, and  $t$  is time. The heat flux vector ( $\bar{q}$ ) and the temperature gradient ( $\nabla T$ ) across a material volume are assumed to occur at the same time. It is assumed that the physical domain for macroscopic models for heat transport is so large that it allows hundreds of thousands of phonon/electron collisions to occur before an observation and description are made for the process of heat transport. Phonon/electron collision requires a finite period of time to take place. Hundreds of thousands of such collisions also imply a sufficiently long time for the process of heat transport to occur. The macroscopic models, therefore, necessitate not only a sufficiently large physical domain for conducting heat, but also a sufficiently long time for heat conduction to take place. From the microscopic point of view, heat transport requires sufficient collisions among energy carriers. The mean free time is of the order of picoseconds for metals. The relaxation time for dielectric crystals and insulators is roughly of the order of nanosecond to picosecond. The transient response to the heat flux from macroscale to microscale will be very different. The lagging behavior in heat transport for the microscale must be considered. In general, the heat transport equations used to describe the thermal behavior at the microscale are expressed as follows:

$$-\nabla \cdot \bar{q} + Q = \rho C_p \frac{\partial T}{\partial t} \quad (1.2)$$

$$\bar{q}(x, y, z, t + \tau_q) = -k\nabla T(x, y, z, t + \tau_\tau) \quad (1.3)$$

where  $\vec{q} = (q_1, q_2, q_3)$  is heat flux,  $T$  is temperature,  $k$  is coefficient of conductivity,  $C_p$  is specific heat,  $\rho$  is the mass density,  $Q$  is heat source,  $\tau_q$  and  $\tau_T$  are positive constants, which are the time lags of the heat flux and temperature gradient, respectively. Clearly, if the scale in one direction is at the submicron, i.e., the order of  $0.1 \mu\text{m}$ , then the heat flux and temperature gradient in this direction will occur at different times, as shown in Equation (1.3).

### **1.3. Research Objective**

As mentioned in the previous discussion, additional physical mechanisms may need to be incorporated to describe the process of heat transport as the transient time shortens. As the transient time becomes comparable to the mean free time of energy carriers, the microscale effect in space needs to be accommodated further because the thermal penetration depth developed in this time frame may cover only several tens of angstroms. For the thin film with a microscale, the conventional Fourier's law will no longer be suitable for describing the heat transport process. The main objective of the research is to develop a hybrid finite element-finite difference method to solve three-dimensional heat transport equations (Equations (1.2) and (1.3)) in double layers with the thickness being in microscale and with a cylindrical domain. The significance of the development is that the method can be used for better describing the heat transport phenomena with an arbitrary domain. Using this method, one can easily predict the temperature profile in a thin film at microscale and with arbitrary geometry. It will provide necessary fundamentals to do the thermal analysis.

#### **1.4. Research Methodology**

To achieve the above objectives, the following developments are pursued:

- (1) Set up the governing equations including the initial and boundary conditions for thermal analysis of a double-layered cylindrical thin film. The lagging consideration in the heat transport process will be considered. The first-order approximation of Equation (1.3) will be used for simplification.
- (2) Discretize the three-dimensional heat transport equation using the finite element and finite difference methods. To this end, the finite element method is first employed to discretize the equations in the x-y directions. The Crank-Nicholson finite difference method is then applied to the z direction.
- (3) Develop a domain decomposition algorithm for thermal analysis of the double-layered cylindrical thin film. To this end, a preconditioned Richardson iteration is first employed to the discretized scheme so that the systems become two block tri-diagonal linear systems with unknown values at the interface. The parallel Gaussian elimination is then applied to the new systems.
- (4) Test the applicability of the method by investigating the temperature rise in double layers where a cylindrical gold thin film is on a cylindrical chromium thin film.

#### **1.5. Outline of the Dissertation**

There are six chapters in this dissertation. Chapter One is the introduction which gives a general overview of the development of the thin film technology and states what the problem is, what the objective is for this research, and what methodology will be used in this research. Chapter Two presents previous research works about this problem.

Several models are discussed. Chapter Three presents the mathematical model. It gives the governing equations for heat transport and stress-strain relations. The choice of the boundary conditions is also discussed. Chapter Four mainly focuses on numerical methods. We start from how to discretize the differential equations; then we discuss how to employ the preconditioned Richardson iteration to obtain two block tri-diagonal linear systems, and finally we describe how to apply a parallel Gaussian elimination procedure to solve these two systems and obtain a domain decomposition algorithm for thermal analysis of a double-layered cylindrical thin film. Chapter Five presents the numerical results for thermal analysis of a gold layer on a chromium padding layer. Chapter Six summarizes the research work.

## CHAPTER 2

### BACKGROUND

Transient response has been a long-time concern in micromanufacturing. In the classical theory of heat diffusion, for example, the major concern lies in the transient behavior of temperature resulting from the time-rate of change of internal energy in transition between thermodynamic states. Such transient behavior varies with the time-dependent boundary conditions or body heating, but the result is always diffusion, no matter how short the response time. Additional physical mechanisms may need to be incorporated to describe the process of heat transport as the transient time shortens. In this chapter, we will review the previous works dealing with the heat transport phenomena in thin films, including several models and the most recent activities. These research works focus on the fundamentals of the heat transport mechanisms and emphasize on the transient response of the heat transport process. After studying this chapter, one will make sense out of why the conventional Fourier's law will not work for the thin films with a microscale thickness.

Before we go any further, two very important quantities must be defined first: the mean free path  $d$  and the mean free time  $\tau$ . Figure 2.1 explains these two concepts.

$$d = \frac{d_1 + d_2 + d_3}{3}$$

$$\tau = \frac{(t_2 - t_1) + (t_3 - t_2) + (t - t_3)}{3} = \frac{t - t_1}{3}$$

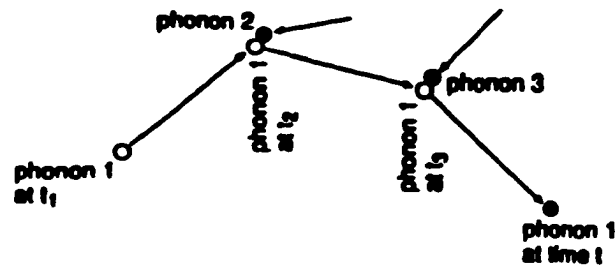


**Figure 2.1** Energy transport through phonon-phonon or phonon-electron collision

As the transient time becomes comparable to the mean free time of energy carriers, the microscale effect in space needs to be accommodated further because the thermal penetration depth developed in this time frame may cover only several tens of angstroms. Consequently, the thermal penetration depth may become comparable to the characteristic length in heat transport. The existing models include (1) the model of phonon-electron interaction in metal films; (2) phonon scattering in dielectric crystals, insulators, and semiconductors; and (3) fracton transport through fractal networks. The approaches used for describing microscale heat transport may have very different physical bases from those in macroscopic phenomenological approaches, exemplified by the semi-classical Boltzmann transport equation, the equation of phonon radiative transport, and the fractal geometry describing the motion of random walks in percolating structures. From the boarder point of view, therefore, the transient response in heat conduction involves more than obtaining the time-dependent solution satisfying a certain energy equation. It also

includes new physical mechanisms, which may involve new philosophical bases in fundamental descriptions that arise in association with shortening of the response time.

Thermal lagging is a special response in time. It provides a phenomenological approach that describes the noninstantaneous response between the heat flux vector and the temperature gradient in the process of the heat transport. The relaxation behavior resides in the phase lag, or time delay, of the heat flux vector. It describes the fast-transient effect of the thermal inertial. The finite time required for the energy exchange/thermal activation in microscale, on the other hand, resides in the phase lags of the temperature gradient. It describes the microstructural interaction effect in space, in terms of the resulting delayed response in time. The two-phase lags interweave in the history of heat transport, resulting in the flux-precedence type of heat flow and the gradient-precedence type of heat flow. The dual-phase-lag model thus developed still employs the continuum concepts such as temperature gradient and the heat flux vector across a representative volume. However, the resulting lagging response seems to be descriptive for several unique features observed in the experimental and analytical results of microscale heat transport. The phase-lag concept is very effective in making the transition from macro- to microscale.

### **2.1. Phonon-Electron Interaction Model**

The phonon-electron interaction for heat transport in metals is explained in Figure 2.2, except phonon-phonon collision should be replaced by phonon-electron collision. The heating mechanism involves excitation of the electron gas and heating of the metal lattice through phonon-electron interaction in short times, called two-step heating process.

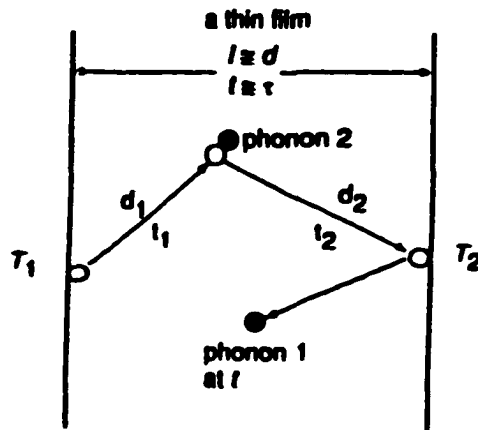


**Figure 2.2** Phonon/electron interaction and scattering in a thin film

Note: The thickness is of the same order of magnitude as the mean free path.

The initial model was proposed by Kaganov et al. (1957) and Anisimov et al. (1974). It was not rigorously proved until being put on a quantum mechanical and statistical basis by Qiu and Tien (1993).

For metals, the two-step model describes heating of the electron gas and the metal lattice by a two-step process. Mathematically, this two-step model can be expressed as follows:

$$C_e \frac{\partial T_e}{\partial t} = \nabla \cdot (k \nabla T_e) - G(T_e - T_l) \quad \text{heating of the electron gas} \quad (2.1)$$

$$C_l \frac{\partial T_l}{\partial t} = G(T_e - T_l) \quad \text{heating of the metal lattice} \quad (2.2)$$

with  $C$  denoting the volumetric heat capacity,  $k$  the thermal conductivity of the electron

gas, and the subscripts e and l standing for electron and lattice, respectively. The externally supplied phonons, such as those from an intensified laser, first increase the temperature of the electron gas according to Equation (2.1). Through phonon-electron interactions, which is the second stage of the heat transport, represented by Equation (2.2), the hot electron gas heats up the metal lattice by phonon-electron interaction. The energy exchange between phonons and electrons is characterized by the phonon-electron coupling factor  $G$  (Kaganov et al., 1957):

$$G = \frac{\pi^2 m_e n_e v_s^2}{6 \tau_e T_e} \quad \text{for } T_e \gg T_l \quad (2.3)$$

where  $m_e$  represents the electron mass,  $n_e$  the number density (concentration) of electrons per unit volume, and  $v_s$  the speed of the sound,

$$v_s = \frac{k}{2\pi\hbar} (6\pi^2 n_a)^{\frac{1}{3}} T_D \quad (2.4)$$

with the quantity  $h$  being the Planck constant,  $k$  being the Boltzmann constant,  $n_a$  being the atomic number density per unit volume, and  $T_D$  representing the Debye temperature. The electron temperature ( $T_e$ ) is much higher than the lattice temperature ( $T_l$ ) in the early-time response. The condition of  $T_e \gg T_l$  in equation (2.3) for the applicability of  $G$  expression is thus valid in the fast-transient process of electron-phonon dynamics. Within the limits of Wiedemann-Frenz's law, which states that for metals at moderate temperatures (roughly for  $T_l > 0.48T_D$ ) the ratio of the thermal conductivity to the electrical conductivity is proportional to the temperature and the constant of proportionality is independent of particular metal (a metal-type-independent constant), the electronic thermal conductivity can be expressed as

$$K = \frac{\pi^2 n_e \kappa^2 \tau_e T_e}{3m_e}, \quad (2.5a)$$

Rearrange Equation (2.5a), resulting in

$$m_e = \frac{\pi^2 n_e \kappa^2 \tau_e T_e}{3k} \quad (2.5b)$$

Substituting Equation (2.5b) into Equation (2.3) for the electron mass gives

$$G = \frac{\pi^4 (n_e v \kappa_s)^2}{18k} \quad (2.6)$$

The phonon-electron coupling factor, therefore, depends on the thermal conductivity and the number density of electron gas. Through the speed of sound, in addition, the coupling factor further depends on the number density of atoms and the Debye temperature. The coupling factor does not show a strong dependence on temperature, and it does not seem to be affected by the electronic relaxation time.

In order to estimate the value of  $G$  according to Equation (2.6), the number density of the electron gas,  $n_e$ , is a key quantity. Qiu and Tien (1992) assumed one free electron per atom for noble metals (silver (Ag) and gold (Au), for example) and employed the s-band approximation for the valence electrons in transition metals. Owing to the relatively heavy mass of the d-band electrons in the valence electrons, only a fraction of the s-band electrons can be viewed as free electrons. The value of  $n_e$ , therefore, is chosen as a fraction of the valence electrons. The phonon-electron coupling factor are thus calculated, and the experimentally measured values are listed in Table 1 for comparison. Except for copper and lead, which may exhibit certain ambiguous transition mechanisms, the s-band approximation seems to agree well with the experimental results. As a general trend, a higher free electron number density and higher Debye temperature would result in

larger value of  $G$  and smaller value of the relaxation time.

**Table 2.1 Phonon-electron coupling factor  $G$  for some noble and transition metals (reproduced from Qiu and Tien (1992))**

Metal	Calculated, $\times 10^{16}$ W/m <sup>3</sup> K	Measured, $\times 10^{16}$ W/m <sup>3</sup> K
Cu	14	4.8 $\pm$ 0.7 (Brorson et al., 1990) 10 (Elsayed-Ali et al., 1987)
Ag	3.1	2.8 (Groeneveld et al., 1990)
Au	2.6	2.8 $\pm$ 0.5 (Brorson et al., 1990)
Cr	45 ( $n_e/n_a = 0.5$ )	42 $\pm$ 5 (Brorson et al., 1990)
W	27 ( $n_e/n_a = 1.0$ )	26 $\pm$ 3 (Brorson et al., 1990)
V	648 ( $n_e/n_a = 2.0$ )	523 $\pm$ 37 (Brorson et al., 1990)
Nb	138 ( $n_e/n_a = 2.0$ )	387 $\pm$ 36 (Brorson et al., 1990)
Ti	202 ( $n_e/n_a = 1.0$ )	185 $\pm$ 16 (Brorson et al., 1990)
Pb	62	12.4 $\pm$ 1.4 (Brorson et al., 1990)

There are two equations and two unknowns. These unknowns can be solved in a coupled manner, or they can be combined to give a single energy equation describing heat transport through phonon-electron interaction in microscale. The combined energy equation, from an alternate point of view, can be derived from the phase-lag concept in the temporal response. Such a coincidence strongly supports the dual-phase-lag model.

Complexity of solutions for Equations (2.1) and (2.2) lies in the temperature-dependent heat capacity of the electron gas, i.e.,  $C_e \equiv C_e(T_e)$ . For an electron-gas temperature lower than the Fermi temperature, which is of the order of  $10^4$  K, the electron heat capacity is proportional to the electron temperature. Such a temperature dependence makes Equations (2.1) and (2.2) nonlinear. For a gold film subjected to femtosecond laser heating, Qiu and Tien (1992) employed the Crank-Nicholson scheme of finite difference to obtain the solutions. With regard to the comparison with the

experimental result, the normalized temperature change in the electron gas is identical to the normalized reflectivity change on the film surfaces:

$$\frac{\Delta R}{(\Delta R)_{\max}} = \frac{\Delta T_e}{(\Delta T_e)_{\max}} \quad (2.7)$$

where  $R$  denotes the reflectivity and the subscript “max” refers to the maximum value occurring in the transient process. The left side of the equation (2.7) can be measured by the front-surface-pump and back-surface-probe technique (Brorson et al., 1987; Elsayed-Ali, 1991; Qiu et al., 1994). The right side of the same equation, on the other hand, can be calculated by solving Equation (2.1) and (2.2) for the electron temperature and normalizing with respect to the maximum value in the transient response at various times. For the gold film subjected to irradiation of a 96 femtosecond (fs,  $10^{-15}$  s) laser with an energy flux of  $1 \text{ mJ/cm}^2$ , the results of reflectivity change at the front surface of the film are reproduced in Figure 2.3 from the work by Qiu and Tien (1992). The time delay marked on the horizontal axis is the time difference between the pump (heating) and the probe (detecting) lasers, which is equivalent to the physical time in the transient response. For both thicknesses of the films, 0.05 and 0.1  $\mu\text{m}$ , the microscopic two-step model accommodating the phonon-electron interaction effect nicely captures the heating ( $0 \leq t \leq 0.096 \text{ ps}$ ) and thermalization ( $0.096 \leq t \leq 3 \text{ ps}$ ) processes of the electron temperature. The temperature level, as expected, increases as the thickness of the film decreases. The classical theory of diffusion, which assumes an immediate equilibrium between phonon (lattice) and electrons and is called the one-step heating model by Qiu and Tien (1992), fails to describe the fast energy transport process. Particularly in the thermalization stage, it overestimates the transient temperature by several times. The transient temperature at

the front surface does not seem to depend on the film thickness according to the diffusion model. The transient temperature remains almost at the same level as the film thickness increases from 0.05 to 0.1  $\mu\text{m}$ . Figure 2.3 shows the transient reflectivity change at the rear surface of the film. The heating and thermalization processes remain similar, with the response times, however, increasing. The time at which the electron temperature reaches its maximum value (the instant of time separating the heating and thermalization stages) increases with film thickness, which is a “wave-like” behavior even under the assumption of diffusion for heat transport through the electron gas. The one-step model completely fails to describe the thermalization process at the rear surface of the film. Unlike the situation shown in Figure 2.3 (the front surface), where at least the qualitative trend was preserved in the same domain of response times, the heating stage predicted by the diffusion model shown in Figure 2.4 (the rear surface) lasts beyond the threshold of 2 ps, resulting in a transient response of reflectivity change that significantly differs from the experimental result both quantitatively and qualitatively. From Figures 2.3 and 2.4 it is clear that, for metals, the microscopic phonon-electron interaction is an important effect to be incorporated for an accurate description of microscale heat transport. In addition to the familiar thermal properties such as heat capacity and thermal conductivity, the phonon-electron coupling factor describing the short-time energy exchange between phonons and electrons is a dominating property in the fast-transient process of laser heating. Along with the equivalent thermal wave speed in the parabolic two-step model, typical values of the phonon-electron coupling factor are listed in Table 2 for copper, gold, silver, and lead. They are of the order of  $10^{16}$ , in units of  $\text{W}/\text{m}^3\text{K}$ , for metals.

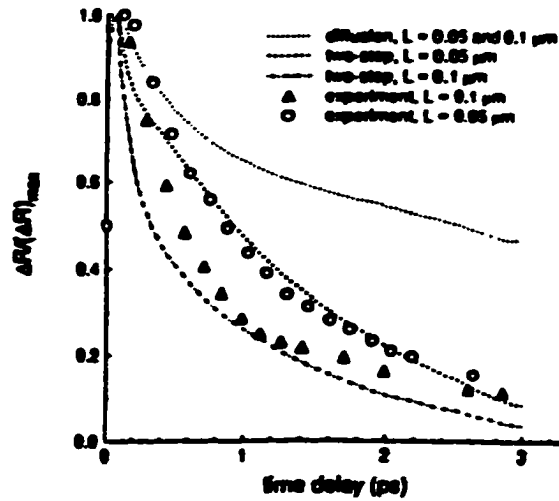


**Figure 2.3** Transient reflectivity change at the front surface of gold films

Note: (thickness 0.05 and 0.1  $\mu\text{m}$ ) subject to laser irradiation (pulse width 96 fs, energy flux 1  $\text{mJ}/\text{cm}^2$ ). Reproduced from the work by Qiu and Tien (1992) with the experimental results obtained by Brorson et al. (1987)

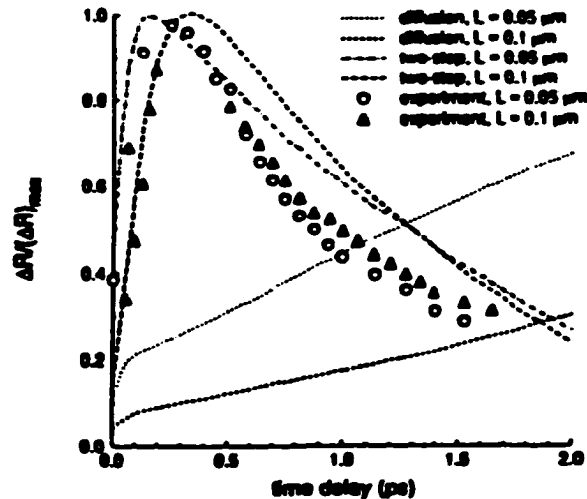


**Figure 2.4** Transient reflectivity change at the rear surface of gold films

Note: (thickness = 0.05 and 0.1  $\mu\text{m}$ ) subject to laser irradiation (pulse width 96 fs, energy flux 1  $\text{mJ}/\text{cm}^2$ ). Reproduced from the work by Qiu and Tien (1992) with the experimental results obtained by Brorson et al. (1987)

Equations (2.1) and (2.2) can be combined to give a single energy equation governing heat transport through the metal lattice or the electron gas (Tzou, 1995a, b). Given their present forms, solving Equations (2.1) and (2.2) for  $T_e$  and  $T_l$  in a simultaneous manner may be more efficient from a numerical point of view. Combining Equations (2.1) and (2.2) together to give a single energy equation describing the electron temperature or the lattice temperature alone, however, is more indicative for the fundamental behavior in microscale heat transport. With emphasis on the characteristics of lattice and electron temperatures, all of the thermal properties, including heat capacities of the electron gas and the metal lattice as well as the thermal conductivity are assumed to be temperature-independent.

A single energy equation governing the lattice temperature can be obtained by eliminating the electron temperature from Equations (2.1) and (2.2). From Equation (2.2), the electron temperature can be expressed in terms of the lattice temperature and its time derivative:

$$T_e = T_l + \frac{C_l}{G} \frac{\partial T_l}{\partial t} \quad (2.8)$$

Substituting Equation (2.8) into Equation (2.1) and using the result of  $G(T_e - T_l)$  from Equation (2.2) results in

$$\nabla^2 T_l + \left(\frac{C_l}{G}\right) \frac{\partial}{\partial t} \nabla^2 T_l = \left(\frac{C_l + C_e}{K}\right) \frac{\partial T_l}{\partial t} + \left(\frac{C_l C_e}{KG}\right) \frac{\partial^2 T_l}{\partial t^2} \quad (2.9)$$

Equation (2.9), governing the lattice temperature alone, introduces a new type of energy equation in conductive heat transfer. It has an usual diffusion term  $(\partial T_l / \partial t)$ , a thermal

wave term  $(\partial^2 T_i / \partial t^2)$ , and a mixed-derivative term  $(\partial[\nabla^2 T_i] / \partial t)$  that reflect the combined effect of microscopic phonon-electron interaction and macroscopic diffusion. In the case that the phonon-electron coupling factor approaches infinity, implying that energy transfer from electrons to phonons is occurring at an infinite rate, Equation (2.9) reduces to the conventional diffusion equation employing Fourier's law, with the coefficient  $(C_e + C_i) / K$  appearing as the equivalent thermal diffusivity.

Similarly, a single energy equation describing the electron temperature can be obtained:

$$T_i = T_e - \frac{k}{G} \nabla^2 T_e + \frac{C_e}{G} \frac{\partial T_e}{\partial t} \quad (2.10)$$

Substituting Equation (2.10) into Equation (2.2) and using the result of  $G(T_e - T_i)$  from Equation (2.1) yields

$$\nabla^2 T_e + \left(\frac{C_i}{G}\right) \frac{\partial}{\partial t} \nabla^2 T_e = \left(\frac{C_i + C_e}{K}\right) \frac{\partial T_e}{\partial t} + \left(\frac{C_i C_e}{KG}\right) \frac{\partial^2 T_e}{\partial t^2} \quad (2.11)$$

Note that both Equation (2.9) and Equation (2.11) have exactly the same form.

## **2.2. Phonon Scattering Model**

Guyer and Krumhansl (1966) solved the linearized Boltzmann equation for the pure phonon field in terms of the eigenvectors of the normal-process, phonon collision/scattering, and the contribution from the electron gas in conducting heat was neglected. The other interactions in which momentum is lost from the phonon system were also neglected in their analysis. The formal solution was represented by two equations

relating the temperature deviation and the heat flux:

$$C_p \frac{\partial T}{\partial t} + \nabla \cdot \bar{q} = 0 \quad (2.12)$$

$$\frac{\partial \bar{q}}{\partial t} + \frac{c^2 C_p}{3} \nabla T + \frac{1}{\tau_R} \bar{q} = \frac{\tau_N c^2}{5} [\nabla^2 \bar{q} + 2\nabla(\nabla \cdot \bar{q})] \quad (2.13)$$

where  $c$  is the average speed of phonons (speed of sound),  $\tau_R$  stands for the relaxation time for the momentum-nonconserving processes and  $\tau_N$  is the relaxation time for normal process in which momentum is conserved in the phonon system. The first equation is the energy equation, while the second is equivalent to Fourier's law in the classical diffusion model and  $CV$  wave equation in the thermal wave model (Cattaneo, 1958; Vernotte, 1958, 1961). The second equation, through a very complicated procedure, is derived from the generalized phonon-thermal-conductivity relation.

All quantities in Equation (2.13) occur at the same instant of time and are ready for further combination with the energy Equation (2.12). Taking divergence of Equation (2.13) and substituting the result for the divergence of the heat flux vector in terms of the time-rate of change of temperature from Equation (2.12) gives

$$\nabla^2 T + \frac{9\tau_N}{5} \frac{\partial}{\partial t} (\nabla^2 T) = \frac{3}{\tau_R c^2} \frac{\partial T}{\partial t} + \frac{3}{c^2} \frac{\partial^2 T}{\partial t^2} \quad (2.14)$$

Equation (2.14) was first derived by Joseph and Preziosi (1989), with emphasis on the interrelation with Jeffrey's type of heat flux equation. It was derived again later by Tzou (1995a) with emphasis on the lagging behavior in microscale.

Regardless of the completely different mechanisms in microscale, it is noteworthy that Equation (2.14), describing heat transport by phonon collision, has exactly the same

form as Equation (2.9) or Equation (2.11), describing heat transport through phonon-electron interaction. The universal form of equations (2.9), (2.11), and (2.14) describing microscale heat transport in various environments stimulates the development of the general ideal of lagging behavior for the fast-transient process of heat transport at small scales.

### **2.3. Phonon Radiative Transfer Model**

The phonon radiative transfer model (PRT) proposed by Majumdar (1993) starts from the same approach as others, employing the solution of the linearized Boltzmann transport equation. The ideal behind the approach, however, is that the PRT describes the Stefan-Boltzmann radiative heat equation for a thin medium and  $CV$  wave equation for a thick medium. Thick or thin is a relative concept compared to the phonon mean free path. Since phonons propagate at the speed of the sound in solids, the mean free path of the phonons is equal to the speed of the sound multiplied by the relaxation time in phonon collision.

Majumdar (1993) derived the one-dimensional heat transport equation of PRT (EPRT for short) from the Boltzmann transport equation. The method he used is the relaxation approximation:

$$\frac{\partial f_{\omega}}{\partial t} + v_x \frac{\partial f_{\omega}}{\partial x} = \left( \frac{\partial f_{\omega}}{\partial t} \right)_{\text{scattering}} \cong \frac{f_{\omega}^0 - f_{\omega}}{\tau} \quad (2.15)$$

where  $f_{\omega}$  denotes the distribution function of phonons with vibrating frequency  $\omega$ ,  $v_x$  is the one-dimensional (assumed to be the  $x$  direction without loss in generality) phonon velocity, and  $\tau$  is the relaxation time (the mean free time in phonon scattering).

Disturbance of the distribution function from its equilibrium state,  $f_{\omega}^0$  in Equation (2.15), results from phonon scattering for the duration of the relaxation time. The scattering term on the right side of Equation (2.15), to the first-order approximation in the short-time transient, can thus be replaced by the amount of deviation of the distribution function divided by the relaxation time. This is called the relaxation-time approximation, popularly used for obtaining the solution of the linearized Boltzmann transport equation.

The heat flux  $\vec{q}$  and the internal energy  $e$  are related to the phonon intensity  $I_{\omega}$  through the following equations:

$$\vec{q} = \iint_{\Omega=4\pi}^{\omega_D} \mu I_{\omega} d\omega d\Omega \quad (2.16a)$$

$$e = \iint_{\Omega=4\pi}^{\omega_D} \frac{I_{\omega}}{v} d\omega d\Omega \quad \text{with } d\Omega = \sin \theta d\theta d\phi \quad (2.16b)$$

with  $\omega_D$  being the Debye cutoff phonon frequency.

The phonon intensity in heat transport,  $I_{\omega}$ , can be obtained by summing up the three phonon polarizations over the distribution function:

$$I_{\omega}(\theta, \phi, x, t) = \sum_p \vec{v}(\theta, \phi) f_{\omega}(x, t) h \omega D(\omega) \quad (2.17)$$

with  $\vec{v}(\theta, \phi)$  denoting the velocity vector of phonons in the direction defined by  $(\theta, \phi)$  in a spherical coordinate system within a solid angle  $d\Omega = \sin \theta d\theta d\phi$ , as shown in Figure 2.5,  $h$  the Planck constant, and  $D(\omega)$  the density of states per unit volume in the frequency domain of lattice vibrations. The projection of the velocity vector onto the x axis is clearly  $v_x = v \cos \theta$ . Multiplying Equation (2.15) by  $v_x h \omega D(\omega)$  and summing up the result over the three phonon polarizations according to Equation (2.17) gives

$$\frac{\partial}{\partial t} \sum_p v_x h\omega D(\omega) f_{\omega} + v_x \frac{\partial}{\partial x} \sum_p v_x h\omega D(\omega) f_{\omega} = \sum_p v_x h\omega D(\omega) \left[ \frac{f_{\omega}^0 - f_{\omega}}{\tau} \right]. \quad (2.18)$$

Denoting

$$v_x = v_{\mu}, \text{ with } \mu = \cos\theta, \text{ and } I_{\omega}^0 = \sum_p v_x h\omega D(\omega) f_{\omega}^0 \quad (2.19)$$

Dividing the entire equation by the phonon speed,  $v$ , Equation (2.18) becomes

$$\frac{1}{v} \frac{\partial I_{\omega}}{\partial t} + \mu \frac{\partial I_{\omega}}{\partial x} = \frac{I_{\omega}^0 - I_{\omega}}{\tau v}, \quad (2.20)$$

with  $v\tau$  being the mean free path in phonon collisions. The right side of Equation (2.20) represents disturbance of an equilibrium state by mutual interactions of phonons.

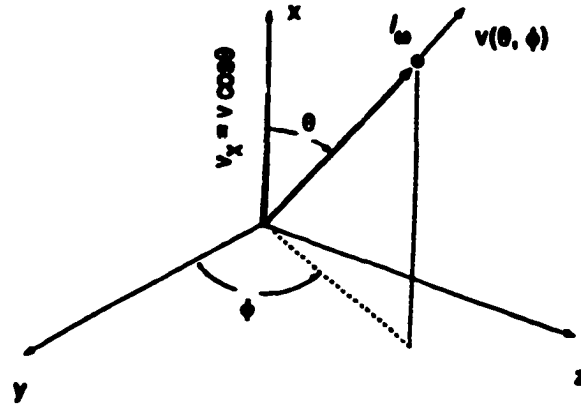


**Figure 2.5** Phonon intensity  $I_{\omega}$  and the azimuthal angle  $\theta$  and  $\phi$  defining the velocity

For phonon transport with azimuthal symmetry in  $\phi$ , in particular,  $q$  and  $e$  result in

$$q = 2\pi \int_{-1}^1 \int_0^{\infty} \mu I_{\omega} d\omega d\mu \quad (2.21a)$$

$$e = 2\pi \int_{-1}^1 \int_0^{\omega_D} \frac{I_\omega}{v} d\omega d\mu \quad (2.21b)$$

based on the phonon intensity  $I_\omega$ .

Multiplying Equation (2.20) by  $2\pi$  and integrating the resulting equation over  $\mu$  and  $\omega$  in the range  $-1 < \mu < 1$  and  $0 < \omega < \omega_D$  gives, with the assistance of Equations (2.21a) and (2.21b),

$$\frac{\partial e}{\partial t} + \frac{\partial q}{\partial x} = 2\pi \int_{-1}^1 \int_0^{\omega_D} \left[ \frac{I_\omega^0 - I_\omega}{\tau v} \right] d\omega d\mu \quad (2.22)$$

Two features need to be noted: (1) The equilibrium intensity function on the right side of Equation (2.22), according to Equation (2.19), is a function of temperature only. (2) The left side of Equation (2.22) is zero definite because it is the one-dimensional form of the energy equation in a rigid conductor. Therefore the phonon intensity function  $I_\omega(x, t, \mu)$ :

$$\frac{1}{v} \frac{\partial I_\omega}{\partial t} + \mu \frac{\partial I_\omega}{\partial x} = \frac{\frac{1}{2} \int_{-1}^1 I_\omega d\mu - I_\omega}{\tau v} \quad (2.23)$$

Once the phonon intensity is obtained, the temperature distribution is obtained from the Bose-Einstein distribution function at an equilibrium state:

$$I_\omega^0(T) = \frac{1}{2} \int_{-1}^1 I_\omega d\mu = \sum_p v_p \frac{h\omega D(\omega)}{\exp\left[\frac{h\omega}{\kappa T(x)}\right] - 1} \quad (2.24)$$

Joshi and Majumdar (1993) solved numerically for the heat transport in a one-dimensional medium by using the explicit upstream differencing method. The detailed mathematical derivation can be found in Dr. Tzou's book "Macro- To Microscale Heat Transfer".

Here let us neglect the mathematical representation and go to the results directly.

Figure 2.6 compares the temperature profiles obtained by the classical diffusion model (macroscopic in both space and time), the *CV* wave model (macroscopic in space but microscopic in time), and the EPRT (microscopic in both space and time). The dimensionless temperature ( $\theta$ ), dimensionless space ( $\delta$ ), and dimensionless time ( $\beta$ ) are defined as

$$\theta = \frac{T - T_0}{T_1 - T_0}, \quad \delta = \frac{x}{L}, \quad \beta = \frac{t}{(l/v)} \quad (2.24)$$

with  $l$  being the effective mean free path,  $\tau = l/v$ .

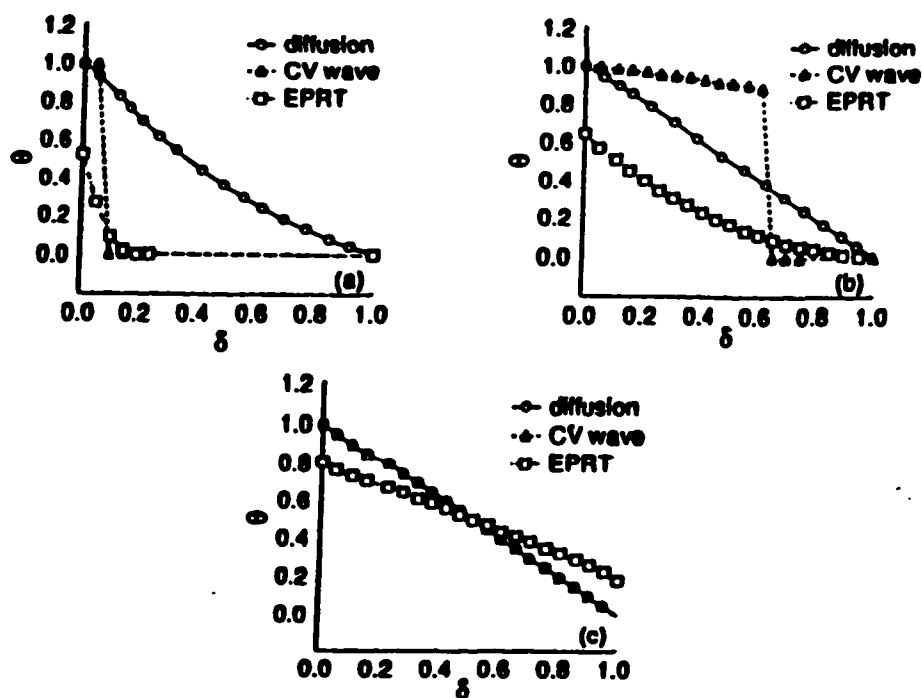


**Figure 2.6** Temperature profiles in 1-D solid predicted by three different models. Note: The models are the classical diffusion, *CV* wave, and EPRT models. Reproduced from the work by Joshi and Majumdar (1993)

The film thickness was taken as  $0.1 \mu\text{m}$  in Figure 2.6. Sharp wavefronts exist in the temperature profiles predicted by the  $CV$  wave mode in Figure 2.6a at  $\beta = 0.1$  and Figure 2.6b at  $\beta = 1.0$ . The macroscopic models in space, including both diffusion and  $CV$  wave models, seem to overestimate significantly the transient temperature. As the transient time lengthens, illustrated by the steady-state distributions shown in Figure 2.6c, the sharp wavefront in the  $CV$  wave model vanishes, while the temperature profile collapses onto that predicted by the diffusion. It is important to note that EPRT does not reduce to the distribution model employing Fourier's law at steady state. According to Figure 2.6c, EPRT predicts a lower temperature level at the high-temperature side ( $x = 0$ ) and a higher temperature at the low-temperature side ( $x = L$ ).

The difference between the EPRT and the diffusion or  $CV$  model at steady state vanishes as the film thickness exceeds the acoustical limit, i.e.,  $L \gg \nu\tau$ . This is illustrated in Figure 2.6 for  $L = 10 \mu\text{m}$ , which is 2 orders of magnitude thicker than the value used in Figure 2.7. The temperature profiles predicted by EPRT, diffusion, and  $CV$  wave models collapse onto each other at steady state, showing a linearly decayed distribution of temperature with respect to  $x$ . In fact, the equations of the macroscopic diffusion and thermal wave models, under the steady-state condition, require the linearly decay distribution.

If the thickness of the thin film is of the same order of magnitude as the effective mean free path, the EPRT developed by Majumdar (1993) results in the following steady-state heat flux:

$$q = \frac{\sigma(T_1^4 - T_0^4)}{\frac{3}{4}\left(\frac{L}{l}\right) + 1} \quad (2.25)$$

with  $\sigma$  denoting the Stefan-Boltzmann constant in radiative heat transfer. This equation describes the transition mode from diffusion to radiative heat transport associated with shrinkage of the film thickness. If  $l \gg L$ , Equation (2.25) reduces to the same form as the Stefan-Boltzmann law in radiative heat transfer. In the transition of the film thickness from “thick” to “thin”, Equation (2.5) may be the most elegant feature in EPRT.

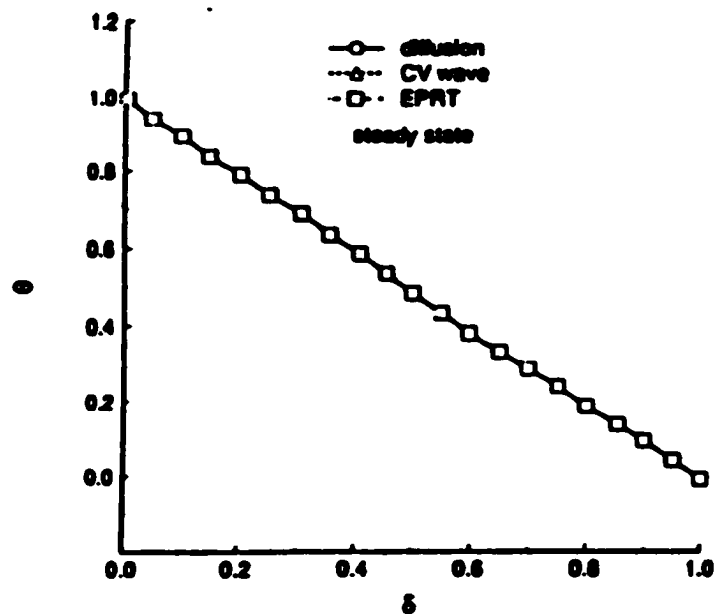


**Figure 2.7** Temperature profiles in 1-D solid predicted by three different models  
 Note: The models are classical diffusion, *CV* wave, and EPRT models. Reproduced from the work by Joshi and Majumdar (1993)

#### 2.4. Dual-Phase-Lag Model

Tzou et al. (1995) considered the case of ultrafast pulse-laser heating on metal films. The ultrafast lasers with a pulse duration of order of picoseconds are used to study

the electron-phonon dynamics in extremely short time. To date, the shortest pulse duration reaches 96 picoseconds (Broson et al., 1987) and 100 picoseconds (Qiu et al., 1994). For high-conducting metals such as gold, the time frame of primary concern is about a few picoseconds, and the penetration depth is of the order of submicrons. The heat transport, therefore, is more complicated under extreme conditions of small scales in both space and time. According to the experimental observations conducted by Qiu et al. (1994), the intensity of the laser beam used is

$$I_s(t, \tau) = C_0 I(t) I(t + \tau) \quad (2.26)$$

The measured light intensity, called autocorrelation of the laser pulse, is

$$I_s(\tau) = C_0 \int_{-\infty}^{\infty} I(t) I(t + \tau) dt \quad (2.27)$$

where  $I(t)$  is the light intensity of the preceding beam,  $I(t + \tau)$  is the light intensity of the delayed beam,  $C_0$  is a crystal constant, and  $\tau$  is the time delay.

Qiu and Tien (1992, 1993, 1994) found that the intensity of laser absorption  $S_0$  is

$$S_0 = 0.94 J \left( \frac{1 - R}{t_p \delta} \right) \quad (2.28)$$

where  $J$  is laser fluence,  $R$  is the radiative reflectivity of the sample to the laser beam,  $t_p$  is the full-width-at-half-maximum pulse duration, and  $\delta_0$  is the penetration depth of laser radiation. Based on the light intensity  $I(t)$ , the volumetric heating,  $S(x, t)$ , in the sample is

$$S(x, t) = S_0 e^{-\frac{x}{\delta}} I(t) \quad (2.29)$$

Selecting Gaussian distribution for the light intensity of laser, i.e.,

$$I(t) = I_0 e^{-\psi \left(\frac{t}{t_p}\right)^2} \quad (2.30)$$

where  $\psi$  is a constant,  $\psi \approx 2.77$ . Substituting Equations (2.28) and (2.29) into Equation (2.27), then the autocorrelation of the laser pulse is

$$I_s(\tau) = C_0 \int_{-\infty}^{\infty} e^{-\psi \left(\frac{t}{t_p}\right)^2} e^{-\psi \left(\frac{t+\tau}{t_p}\right)^2} dt = [C_0 I_0^2 \sqrt{\frac{\pi t_p^2}{2\psi}}] e^{-\frac{\psi}{2} \left(\frac{\tau}{t_p}\right)^2} \quad (2.31)$$

The bracketed term is  $I_s(0)$ . The normalized autocorrelation of the laser pulse is

$$\frac{I_s(\tau)}{I_s(0)} = e^{-\frac{\psi}{2} \left(\frac{\tau}{t_p}\right)^2} = e^{-2 \ln 2 \left(\frac{\tau}{t_p}\right)^2} \quad (2.32)$$

There are other forms of light intensity. Selecting Gaussian distribution is for the purpose of directly using the semi-implicit Crank-Nicholson scheme. Tzou selected a particular form of light intensity that not only yields an autocorrelation of laser pulse comparable to the experimental result but also facilitates the direct use of the Riemann-sum approximation for the Laplace inversion. The ideal light intensity must possess a maximum at  $t = 0$ , a characteristic in the Gaussian profile shown in Equation (2.30). A possibility possessing this property is

$$I(t) = I_0 e^{-a \left|\frac{t}{t_p}\right|} \quad \text{with } a \geq 0, \quad t_p \geq 0 \quad (2.33)$$

The autocorrelation of the laser pulse corresponding to Equation (2.31) is, from Equation (2.27),

$$I_s(\tau) = C_0 I_0^2 \int_{-\infty}^{\infty} e^{-a|t|} e^{-a|t-\tau|} dt \quad \text{with } \psi = \frac{a}{t_p} > 0. \quad (2.34)$$

$$I_s(\tau) = C_0 I_0^2 \left[ \int_{-\infty}^{-\tau} e^{a\tau} e^{a(t-\tau)} dt + \int_{-\tau}^0 e^{a\tau} e^{-a(t+\tau)} dt + \int_0^{\infty} e^{-a\tau} e^{-a(t+\tau)} dt \right], \quad \text{for } \tau \geq 0 \quad (2.35)$$

$$I_s(\tau) = C_0 I_0^2 \left[ \int_{-\infty}^0 e^{\psi t} e^{\psi(t+\tau)} dt + \int_0^{-\tau} e^{-\psi t} e^{\psi(t+\tau)} dt + \int_{-\tau}^{\infty} e^{-\psi t} e^{-\psi(t+\tau)} dt \right], \text{ for } \tau < 0 \quad (2.36)$$

Integrating the right sides of Equation (2.35) and Equation (2.36), then

$$I_s(\tau) = \begin{cases} C_0 I_0^2 \left( \frac{e^{-\psi\tau}}{\psi} + \tau e^{-\psi\tau} \right) & \text{for } \tau \geq 0 \\ C_0 I_0^2 \left( \frac{e^{\psi\tau}}{\psi} - \tau e^{\psi\tau} \right) & \text{for } \tau < 0 \end{cases} \quad (2.37)$$

or

$$\frac{I_s(\tau)}{I_s(0)} = \begin{cases} e^{-\psi\tau} + \psi\tau e^{-\psi\tau} & \text{for } \tau \geq 0 \\ e^{\psi\tau} - \psi\tau e^{\psi\tau} & \text{for } \tau < 0 \end{cases} \quad (2.38)$$

Figure 2.8 shows the comparison of the normalized autocorrelation of the laser pulse, Equation (2.38), Equation (2.32), and the experiment result.

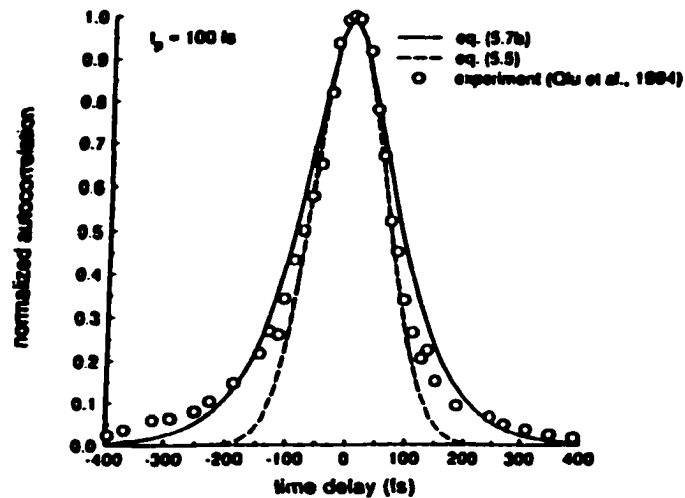


**Figure 2.8** Comparison of the normalized autocorrelation of the laser pulse and others (Equation (2.38), Equation (2.32)(Gaussian distribution), and the experiment result at  $a=1.88$ ,  $t_p=100$  fs.) (reproduced from Qiu et al., 1994)

In dealing with the microscopic phonon-electron interaction, Qiu and Tien (1994) accounted for the temperature-dependent heat capacity of electron gas and thermal conductivity in their effort to model the two-step process of energy transport between phonons and electrons in the short-time transient:

$$C_e(T_e) \frac{\partial T_e}{\partial t} = \frac{\partial}{\partial x} \left( \frac{T_e}{T_l} k \frac{\partial T_e}{\partial x} \right) - G(T_e - T_l) + S \quad (2.39)$$

$$C_l \frac{\partial T_l}{\partial t} = G(T_e - T_l). \quad (2.40)$$

It is a one-dimensional simulation, and the Gaussian profile is employed. The boundary conditions are imposed as in Equation (2.41). It is assumed that heat is not lost from the front and the back surfaces of the film because the laser heating occurs in a very short period of time.

$$\frac{\partial T_e}{\partial x}(0, t) = \frac{\partial T_e}{\partial x}(L, t) = \frac{\partial T_l}{\partial x}(0, t) = \frac{\partial T_l}{\partial x}(L, t) = 0 \quad (2.41)$$

with  $L$  denoting the film thickness. The initial conditions for both the electron and the metal lattice at  $t = -2t_p$  are

$$T_e(x, -2t_p) = T_l(x, -2t_p) = T_0. \quad (2.42)$$

Qiu and Tien solved the one-dimensional model by employing the semi-implicit Crank-Nicholson finite difference scheme. The results, shown in Figure 2.9, agree with the experimental data very well.

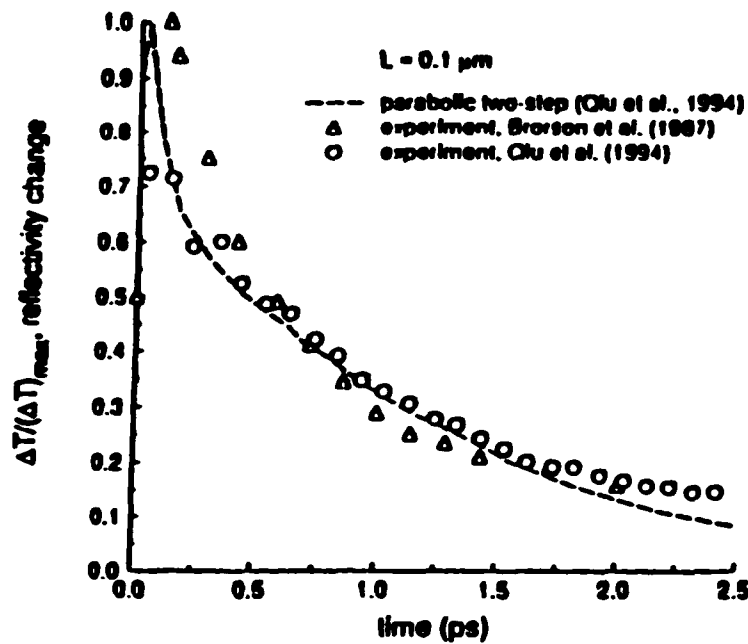


**Figure 2.9** Experimental results of reflectivity change

By Borson et al. (1987) and Qiu et al. (1994) at the front surface of a gold film of thickness  $0.1 \mu\text{m}$ , and predictions from the parabolic two-step model (Qiu et al. 1994).

Tzou studied the lagging behavior by considering the two-step heating process, i.e., the microscopic phonon-electron interaction model. Similar to the discussion in Section 2.1, Equations (2.43) and (2.44) are governing the heat transport through the metal lattice and electron gas, respectively.

$$\nabla^2 T_l + \frac{\alpha_e}{C_E^2} \frac{\partial}{\partial t} (\nabla^2 T_l) = \frac{1}{\alpha_E} \frac{\partial T_l}{\partial t} + \frac{1}{C_E^2} \frac{\partial^2 T_l}{\partial t^2}, \quad (2.43)$$

$$\nabla^2 T_e + \frac{\alpha_e}{C_E^2} \frac{\partial}{\partial t} (\nabla^2 T_e) = \frac{1}{\alpha_E} \frac{\partial T_e}{\partial t} + \frac{1}{C_E^2} \frac{\partial^2 T_e}{\partial t^2} \quad (2.44)$$

Note that (1) the diffusion is assumed for heat transport through the electron gas, but a wave term (the second-order derivative with respect to time) does exist in these equations. The phonon-electron coupling factor  $G$  is equivalent to the speed of thermal wave. The conventional Fourier's law is of the same form of Equations (2.43) and (2.44) as the  $G$  goes to an infinite value, implying either the energy transport from electrons to phonons occurring at zero time or electrons and phonons colliding with each other at an infinite frequency. (2) Under a finite value of  $G$ , the mixed-derivative term and the wave term in Equations (2.43) and (2.44) must exist simultaneously. The mixed-derivative term would disappear if either thermal conductivity of the electron gas went to zero or the heat capacity of the electron gas went to infinity. (3) The coefficient in front of the mixed-derivative term has a dimension of time, and the coefficient in front of the wave term can be expressed as the ratio of another characteristic time to the equivalent thermal diffusivity. These two characteristic times can be viewed as the time lags of the temperature gradient and the heat flux in the fast-transient process in microscale.

By using Laplace transformation and the Riemann sum for the inversion, Tzou has solved these equations. His numerical results have been compared with the experimental results by Brorson et al. (1987) and Qiu et al. (1994) and show an excellent agreement.

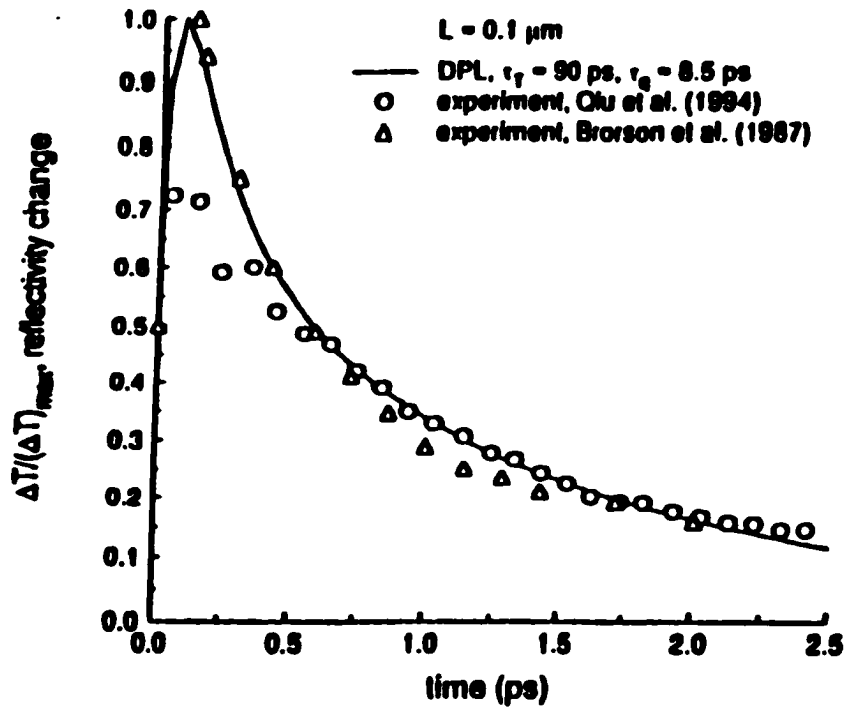


**Figure 2.10.** Normalized temperature change (reflectivity change) in gold film predicted by the dual-phase-lag model. (Comparison with the experimental results by Broson et al. (1987) and Qiu et al. (1994).)

### 2.5. Double-Layered Thin Films

Tzou also studied the double-layered thin film case. Figure 2.11 shows the experimental setup, and Figure 2.12 represents the three-dimensional configuration of a double-layered thin film. The surface layer is a film with a superior reflectivity. The typical example is the use of gold film. A padding layer next to the surface layer is chosen for the purpose of directly resisting laser impingement. Using a double-layered structure of certain materials will enable us to avoid thermal damage.

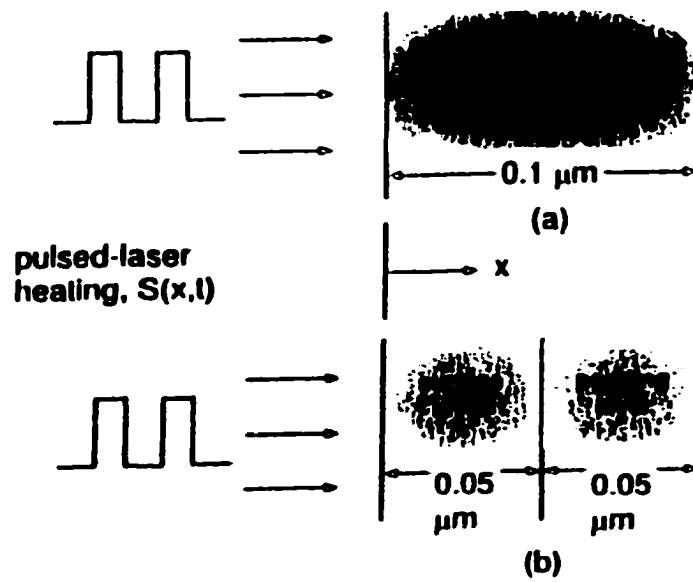


**Figure 2.11.** A padding layer made of different material placed behind the surface layer

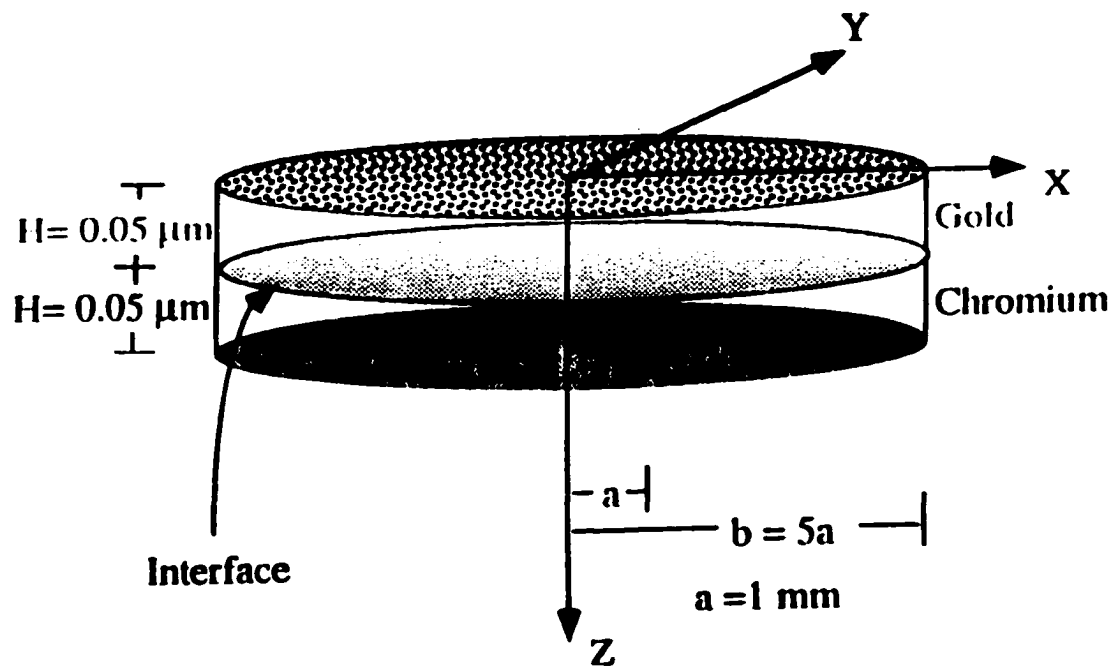


**Figure 2.12.** 3-D configuration of a double layered thin film.

Tzou considered the one-dimensional case and assumed that no heat losses from the film surfaces in the short-time response, that is

$$q_{(1)} = 0 \text{ at } x = 0 \text{ and } q_{(2)} = 0 \text{ at } x = L \quad (2.45)$$

where  $L$  is the thickness for both layers. The subscript (1) and (2) refer to surface layer and padding layer, respectively. Continuity of both temperature and heat flux vector across the interface,  $x = L/2$ , is imposed, implying

$$T_{(1)} = T_{(2)}, \quad q_{(1)} = q_{(2)} \quad \text{at } x = L/2 \quad (2.46)$$

The governing equations now should be

the surface layer,  $x \in [0, L/2]$  —

$$q_{(1)} + \tau_{q(1)} \frac{\partial q_{(1)}}{\partial t} = -\kappa_{(1)} \left[ \frac{\partial T_{(1)}}{\partial x} + \tau_{T(1)} \frac{\partial^2 T_{(1)}}{\partial t \partial x} \right], \quad (2.48a)$$

$$-\frac{\partial q_{(1)}}{\partial x} + S(x, t) = C_{p(1)} \frac{\partial T_{(1)}}{\partial t}. \quad (2.48b)$$

the padding layer,  $x \in [L/2, L]$  —

$$q_{(2)} + \tau_{q(2)} \frac{\partial q_{(2)}}{\partial t} = -\kappa_{(2)} \left[ \frac{\partial T_{(2)}}{\partial x} + \tau_{T(2)} \frac{\partial^2 T_{(2)}}{\partial t \partial x} \right], \quad (2.49a)$$

$$-\frac{\partial q_{(2)}}{\partial x} + S(x, t) = C_{p(2)} \frac{\partial T_{(2)}}{\partial t}. \quad (2.49b)$$

and  $S(x, t)$  is

$$S(x, t) = 0.94 J \left( \frac{1-R}{t_p \delta} \right) e^{-\frac{x}{\delta} - \frac{q(t-2t_p)}{t_p}} \quad (2.50)$$

Therefore, the initial conditions can be expressed as follows:

$$T_{(i)}(x, 0) = T_0 \quad \text{and} \quad \frac{\partial T_{(i)}}{\partial t}(x, 0) = 0 \quad \text{for } i = 1, 2 \quad (2.51)$$

$$q_{(1)}(x,0) = q_{(2)}(x,0) = -\delta S_0 e^{-\frac{x}{\delta} - 2a} \equiv q_0(x,0) \quad (2.52)$$

Using Laplace transformation and the Riemann sum for the inversion, Tzou solved this one-dimensional problem. The detailed mathematical treatment is shown in his book entitled “Macro- to Microscale Heat Transfer.” His numerical results have been compared with the experimental results and show an excellent agreement.

### **2.6. Dai and Nassar’s Work**

Although Tzou’s method is useful for handling one-dimensional situations, for a three-dimensional case, it becomes difficult because Laplace transformation is very complicated. Dai and Nassar also studied the same problem with the same boundary and initial conditions, but they extended the discussion to a three-dimensional case. They considered a three-dimensional rectangular domain (Figure 2.13) and obtained the governing equations below:

$$-\left(\frac{\partial q_1^{(l)}}{\partial x} + \frac{\partial q_2^{(l)}}{\partial y} + \frac{\partial q_3^{(l)}}{\partial z}\right) + Q^{(l)} = \rho^{(l)} C_p^{(l)} \frac{\partial T^{(l)}}{\partial t}, \quad (2.53)$$

$$q_1^{(l)} = -k^{(l)} \frac{\partial T^{(l)}}{\partial x}, \quad (2.54)$$

$$q_2^{(l)} = -k^{(l)} \frac{\partial T^{(l)}}{\partial y}, \quad (2.55)$$

$$q_3^{(l)} + \tau_q^{(l)} \frac{\partial q_3^{(l)}}{\partial t} = -k^{(l)} \left[ \frac{\partial T^{(l)}}{\partial z} + \tau_r^{(l)} \frac{\partial}{\partial t} \left( \frac{\partial T^{(l)}}{\partial z} \right) \right], \quad (2.56)$$

Omitting  $l$ , denoting  $q_3$  as  $q$ , and substituting Equations (2.54) and (2.55) into Equation (2.53) they got

$$\rho C_p \frac{\partial T}{\partial t} = k \left( \frac{\partial^2 T}{\partial x^2} + \frac{\partial^2 T}{\partial y^2} \right) - \frac{\partial q}{\partial z} + Q \quad (2.57)$$

$$q + \tau_q \frac{\partial q}{\partial t} = -k \left[ \frac{\partial T}{\partial z} + \tau_T \frac{\partial}{\partial t} \left( \frac{\partial T}{\partial z} \right) \right] \quad (2.58)$$

They then developed a finite difference method to solve the equations as follows:

Let  $T_{ijk}^n$  denote  $T(i\Delta x, j\Delta y, k\Delta z, n\Delta t)$ , where  $\Delta x$ ,  $\Delta y$ ,  $\Delta z$ , and  $\Delta t$  are the x, y, z directional spatial and temporal mesh sizes, respectively,  $i, j, k = 0, 1, \dots, N+1$  and  $(N+1)\Delta x = (N+1)\Delta y = 1\text{mm}$ ,  $(N+1)\Delta z = 0.1\mu\text{m}$ , while  $q_{ijk}^n = q(i\Delta x, j\Delta y, k\Delta z, n\Delta t)$ ,  $i, j = 1, 2, \dots, N$  and  $k = 1, 2, \dots, N+1$ . An operator  $\delta_x^2$  was defined as

$$\delta_x^2 T_{ijk}^n = \frac{1}{\Delta x^2} (T_{i+1,j,k}^n - 2T_{ijk}^n + T_{i-1,j,k}^n).$$

Using a Crank-Nicholson type of finite difference, they obtained

$$\begin{aligned} \rho C_p \frac{T_{ijk}^{n+1} - T_{ijk}^n}{\Delta t} &= \frac{k}{2} (\delta_x^2 + \delta_y^2) (T_{ijk}^{n+1} + T_{ijk}^n) \\ &\quad - \frac{1}{2\Delta z} (q_{ijk+1}^{n+1} - q_{ijk}^{n+1} + q_{ijk+1}^n - q_{ijk}^n) + Q_{ijk}^{n+\frac{1}{2}} \end{aligned} \quad (2.59)$$

And, they employed a preconditioned Richardson iteration to simplify the equations. A parallel Gaussian elimination procedure was then applied to solve the systems, and a domain decomposition algorithm for thermal analysis of three-dimensional double-layered thin films was obtained. The details were shown by Dai and Nassar et al. (2000). Many of these methods will be used in this dissertation. Therefore I will discuss them in the later chapters. Here, only the numerical results of their research are presented in Figure 2.14 and Figure 2.15.

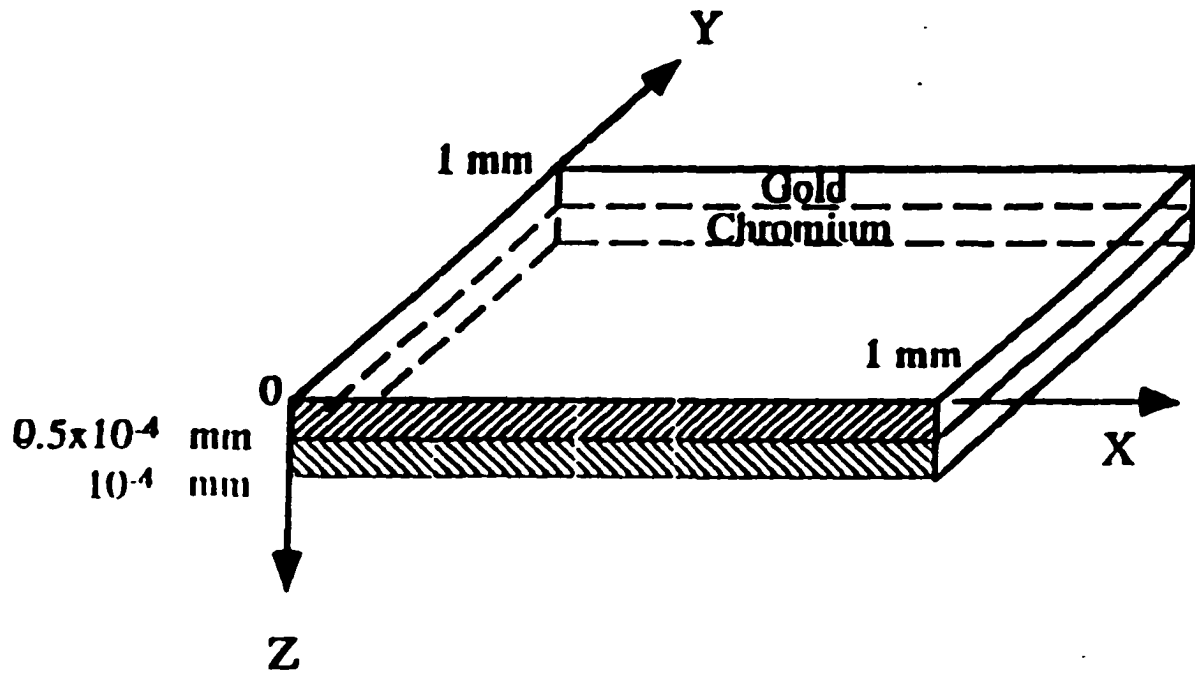


**Figure 2.13.** 3-D configuration of double-layered thin film with a rectangular shape.

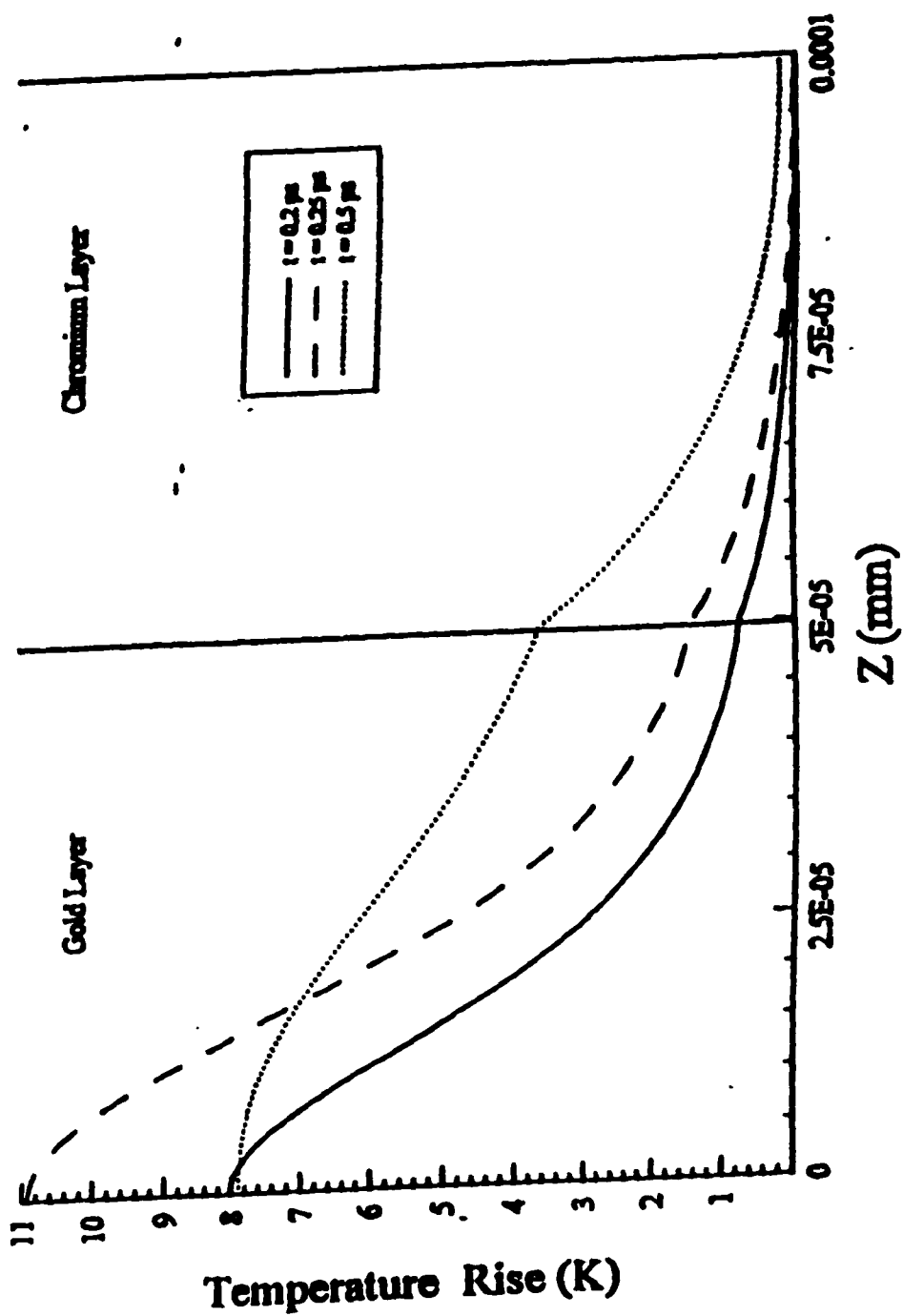
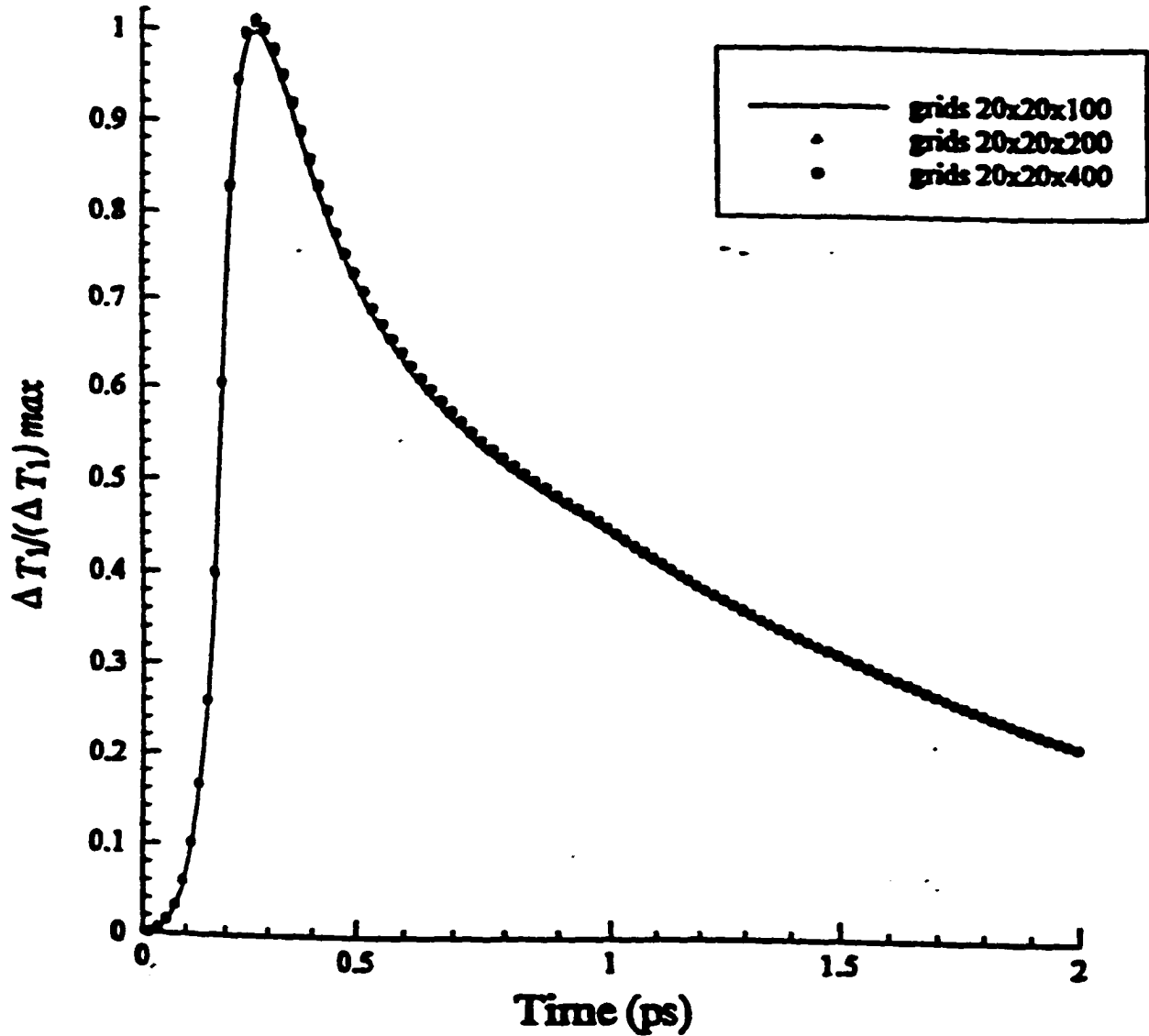


Figure 2.14. Temperature profile along the vertical line.  
 Note:  $x=0.05$  mm and  $y=0.05$  mm. The mesh is  $20 \times 20 \times 200$  with a time increment of 0.005 ps.



**Figure 2.15.** Temperature change on the surface of the gold layer.

Note: The maximum temperature rise ( $T1 \text{ Max}=10.98\text{K}$ ) was obtained using a grid of  $20 \times 20 \times 100$ .

The most significant numerical methods done in solving the heat transport equations at the microscale have been reviewed. Despite the success in the numerical methods, there are still many challenging problems in numerical solutions for heat transport problems. For instance, when the geometry of the thin film is arbitrary, other numerical methods are needed.

## **CHAPTER 3**

### **MATHEMATICAL MODEL**

Chapter Three has four components: the governing equations for temperature distribution; the boundary conditions; the initial conditions; and the relationships among stresses, strains, and temperature distribution. In discussing the governing equations, we first discuss the difference between the macroscopic point of view and the microscopic point of view, and then derive the modified Fourier's law based on the two-step heat transport model.

#### **3.1. Governing Equations for Temperature Distribution**

From the macroscopic point of view, heat transport phenomena can be described by Fourier's law:

$$\vec{q}(x, y, z, t) = -k\nabla T(x, y, z, t) \quad (3.1)$$

where  $\vec{q} = (q_1, q_2, q_3)$  is heat flux,  $T$  is temperature,  $k$  is coefficient of conductivity, and  $t$  is time. The heat flux vector ( $\vec{q}$ ) and the temperature gradient ( $\nabla T$ ) across a material volume are assumed to occur at the same time. For a submicron situation, however, the classical heat diffusion equation is not suitable to describe the heat transport behavior. From the microscopic point of view, heat transport requires sufficient collisions among energy carriers. As the transient time becomes comparable to the mean free time of

energy carriers, the microscale effect in space needs to be accommodated further because the thermal penetration depth developed in this time frame may cover only several tens of angstroms. The time lags for the heat flux and the temperature gradient, as discussed in Chapter Two, will result in an inequality between  $\bar{q}(x, y, z, t)$  and  $-k\nabla T(x, y, z, t)$ .

Therefore, the conventional Fourier's law must be modified as follows:

$$\bar{q}(x, y, z, t + \tau_q) = -k\nabla T(x, y, z, t + \tau_T) \quad (3.2)$$

where  $\bar{q} = (q_1, q_2, q_3)$  is heat flux with  $q_1$ ,  $q_2$ , and  $q_3$  being the components of the heat flux  $\bar{q}$  in the  $x$ ,  $y$ , and  $z$  directions, respectively.  $T$  is temperature,  $k$  is coefficient of conductivity,  $\tau_q$  and  $\tau_T$  are positive constants, which are the time lags of the heat flux and temperature gradient, respectively. Clearly, if the scale in one direction is at the submicronscale, i.e., the order of  $0.1 \mu\text{m}$ , then the heat flux and temperature gradient in this direction will occur at different times, as shown in Equation (3.2).

Using Taylor series to expand  $\bar{q}(x, y, z, t + \tau_q)$  with respect to  $\tau_q$ , then

$$\bar{q}(x, y, z, t + \tau_q) = \bar{q} + \tau_q \frac{\partial \bar{q}}{\partial t} + \dots \quad (3.3)$$

Similarly,

$$-k\nabla T(x, y, z, t + \tau_T) = -k\{[\nabla T + \tau_T[\nabla T]] + \dots\} \quad (3.4)$$

The first-order approximation of Equation (3.3) and (3.4) is

$$\bar{q} + \tau_q \frac{\partial \bar{q}}{\partial t} = -k[\nabla T + \tau_T \frac{\partial}{\partial t}[\nabla T]] \quad (3.5)$$

Tzou et al. (1996) have studied the lagging behavior by solving Equation (3.5) in one dimension in double-layered thin films with the thickness of  $0.05 \mu\text{m}$  each. The solution was obtained by using the Laplace transformation method and the Riemann-sum

approximation for the inversion. In reality, the three-dimensional case should be studied because the heat source may not be even, if the laser irradiates only part of the surface. Clearly we are talking about a three-dimensional case now. The physical configuration used in this study is a double-layered three-dimensional thin film with each thickness being  $0.05 \mu\text{m}$ , while the radius in the x-y directions being one millimeter, as shown in Figure 3.1.

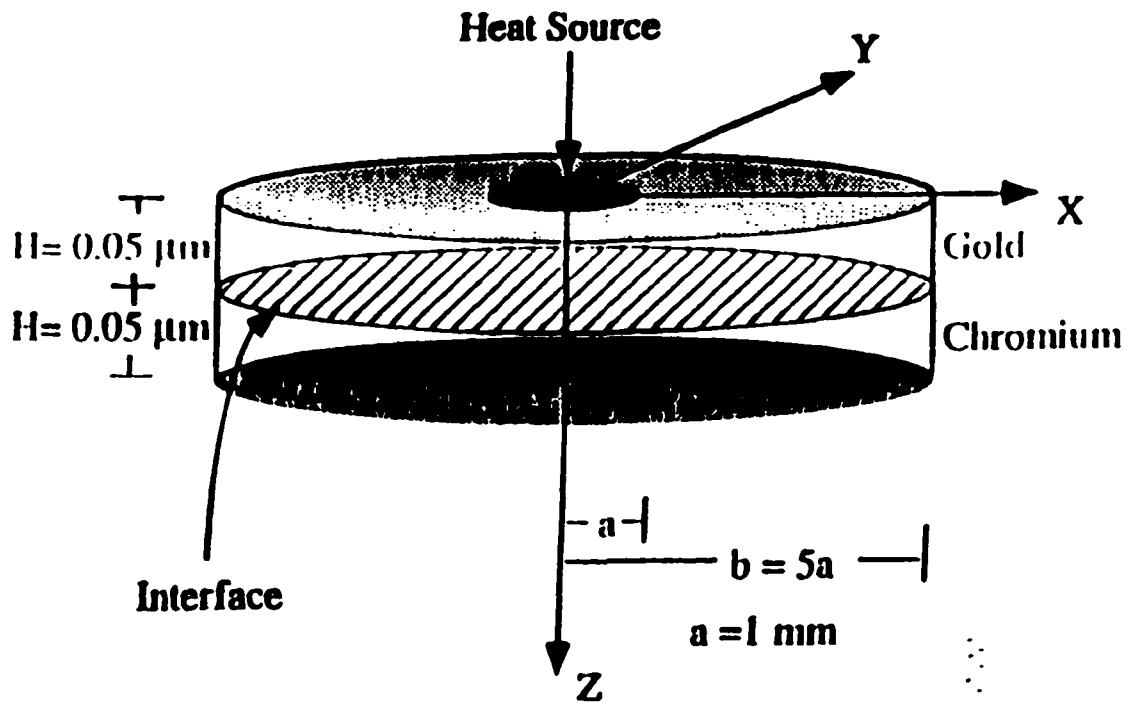


**Figure 3.1. Configuration of 3-D double-layered film.**

Note: Each thickness is  $0.05 \mu\text{m}$ , while the radius in the x-y directions is  $1.0 \text{ mm}$ .

Equation (3.5), coupled with the law of energy conservation, will provide us the complete set of governing equations for the temperature distribution, i.e.,

$$\bar{q} + \tau_q \frac{\partial \bar{q}}{\partial \alpha} = -k[\nabla T + \tau_r \frac{\partial}{\partial \alpha}[\nabla T]] \quad (3.5)$$

$$-\nabla \cdot \bar{q} + Q = \rho C_p \frac{\partial T}{\partial \alpha} \quad (3.6)$$

Since the radius of the x-y domain is of the order of 1 millimeter, the heat flux of the x and y components satisfies the conventional Fourier's law. Only in the z direction must the lagging effect be accounted for. Hence, the governing equations for thermal analysis of a double-layered thin film can be expressed as follows:

$$-\left(\frac{\partial q_1^{(l)}}{\partial x} + \frac{\partial q_2^{(l)}}{\partial y} + \frac{\partial q_3^{(l)}}{\partial z}\right) + Q^{(l)} = \rho^{(l)} C_p^{(l)} \frac{\partial T^{(l)}}{\partial \alpha}, \quad (3.7)$$

$$q_1^{(l)} = -k^{(l)} \frac{\partial T^{(l)}}{\partial x}, \quad (3.8)$$

$$q_2^{(l)} = -k^{(l)} \frac{\partial T^{(l)}}{\partial y}, \quad (3.9)$$

$$q_3^{(l)} + \tau_q^{(l)} \frac{\partial q_3^{(l)}}{\partial \alpha} = -k^{(l)} \left[ \frac{\partial T^{(l)}}{\partial z} + \tau_r^{(l)} \frac{\partial}{\partial \alpha} \left( \frac{\partial T^{(l)}}{\partial z} \right) \right]; \quad (3.10)$$

where  $l = 1, 2$ , which represent the first and second layers, respectively.

### 3.2. The Boundary Conditions

At the interface, continuity of both temperature and heat flux across the interface is imposed. This implies

$$T^{(1)} = T^{(2)} \quad (3.11)$$

$$q_3^{(1)} = q_3^{(2)} \quad (3.12)$$

The boundary conditions are assumed to be  $q_3^{(1)} = 0$  on the top surface,  $q_3^{(2)} = 0$  on the

bottom surface, and  $\frac{\partial T^{(t)}}{\partial \bar{\nu}} = 0$  or  $T^{(t)} = T_{\infty}$  on the lateral walls,  $\nu$  is the unit normal vector and  $T_{\infty}$  is the surrounding temperature. These assumptions do make sense to us because we are using an ultrafast pulse-laser that has a duration of the order of picoseconds. It is assumed that heat is not lost from the front and the back surfaces of the film because the laser heating occurs in a very short period of time.

### **3.3. The Initial Conditions**

The initial conditions are assumed to be

$$T^{(t)} = T_0 \quad \text{and} \quad \frac{\partial T^{(t)}}{\partial x} = 0 \quad (3.13)$$

$$q^{(t)} = q_0^{(t)}(x, y, z) \quad (3.14)$$

where  $T_0$  and  $q_0^{(t)}$  are constants.

### **3.4. Governing Equations for Stresses and Strains**

As mentioned in the previous chapter, stress, strain, and temperature are interrelated in a very complicated manner. The exact solution of problems of general thermoelasticity presents, therefore, enormous difficulties, and the number of known solutions is very small. Fortunately, however, drastic simplifications of the basic equations are possible in many cases of practical interest.

#### **3.4.1 Physics Equations**

The following equations represent the interrelation of stress, strain, and

temperature.

$$\epsilon_x = \frac{1}{E}[(1+\nu)\sigma_x - \nu(\sigma_x + \sigma_y + \sigma_z)] + (1-2\nu)k_s T \quad (3.15)$$

$$\epsilon_y = \frac{1}{E}[(1+\nu)\sigma_y - \nu(\sigma_x + \sigma_y + \sigma_z)] + (1-2\nu)k_s T \quad (3.16)$$

$$\epsilon_z = \frac{1}{E}[(1+\nu)\sigma_z - \nu(\sigma_x + \sigma_y + \sigma_z)] + (1-2\nu)k_s T \quad (3.17)$$

$$\gamma_{xy} = \frac{1+\nu}{E}\tau_{xy}, \quad \gamma_{xz} = \frac{1+\nu}{E}\tau_{xz}, \quad \gamma_{yz} = \frac{1+\nu}{E}\tau_{yz}, \quad (3.18)$$

where  $\sigma_x, \sigma_y, \sigma_z, \tau_{xy}, \tau_{xz}, \tau_{yz}$  are normal and tangent stress tensors in the  $x, y, z$  directions, respectively.  $\epsilon_x, \epsilon_y, \epsilon_z, \gamma_{xy}, \gamma_{xz}, \gamma_{yz}$  are normal and tangent strain tensors,  $\nu$  is the Poisson's ratio,  $E$  is the Young's modulus.

### 3.4.2 Differential Equations

The differential equations are based on Newton's second law:

$$\rho \frac{\partial^2 u}{\partial t^2} = \frac{\partial \sigma_x}{\partial x} + \frac{\partial \tau_{xy}}{\partial y} + \frac{\partial \tau_{xz}}{\partial z} \quad (3.19)$$

$$\rho \frac{\partial^2 v}{\partial t^2} = \frac{\partial \sigma_y}{\partial y} + \frac{\partial \tau_{xy}}{\partial x} + \frac{\partial \tau_{yz}}{\partial z} \quad (3.20)$$

$$\rho \frac{\partial^2 w}{\partial t^2} = \frac{\partial \sigma_z}{\partial z} + \frac{\partial \tau_{xz}}{\partial x} + \frac{\partial \tau_{yz}}{\partial y} \quad (3.21)$$

### 3.4.3 Geometry Equations

$$\epsilon_x = \frac{\partial u}{\partial x}, \quad \epsilon_y = \frac{\partial v}{\partial y}, \quad \epsilon_z = \frac{\partial w}{\partial z} \quad (3.22)$$

$$\gamma_{xy} = \frac{\partial v}{\partial x} + \frac{\partial u}{\partial y}, \quad \gamma_{xz} = \frac{\partial w}{\partial x} + \frac{\partial u}{\partial z}, \quad \gamma_{yz} = \frac{\partial v}{\partial z} + \frac{\partial w}{\partial y} \quad (3.23)$$

**These relations link the stress, strain, and temperature distribution together. Knowing these equations will provide us a mean to solve the stress-strain problems. Therefore, we can focus on solving the temperature distribution only.**

## **CHAPTER 4**

### **NUMERICAL METHOD**

Although the governing equations for thermal analysis of three-dimensional heat transport in a double-layered thin film are obtained, they are difficult to solve analytically. In fact, the analytic solutions for these partial differential equations describing the heat transport process cannot be obtained because of the complication of the three-dimensional domain. Tzou's approach, using Laplace transformation and Riemann-sum for the inversion, is complicated for a three-dimensional case. Also, we will have to face the fact that the value at the interfacial boundary between the layers is unknown. Drs. Dai and Nassar have considered the three-dimensional heat transport equations in a double-layered thin film with microscale thickness and a rectangular domain. The equations are solved by using a finite difference scheme as described in Section 2.6. But, for an arbitrary geometry, a new method must be developed because the finite difference method is relatively suitable for regular geometry. Since the finite element method handles arbitrary boundary conditions nicely, the  $x$ - $y$  domain has been discretized by the use of finite elements. The cross-section of  $x$ - $z$  plane, on the other hand, is still a rectangular shape. Therefore, the finite difference method will be used.

In this chapter, the finite element basis, Crank-Nicholson method, preconditioned Richardson iterative procedure, and a domain decomposition method will be discussed.

#### **4.1. Introduction to Finite-Element Method**

Many physical problems have boundary conditions involving derivatives and irregularly shaped boundaries. Boundary conditions of this type are difficult to handle using finite-difference techniques because each boundary condition involving a derivative must be approximated by a difference quotient at the grid points, and irregular shaping of the boundary makes placing the grid points difficult. The finite-element method includes the boundary conditions as integrals in a functional that is minimized, so the construction procedure is independent of the particular boundary conditions of the problem.

The finite element discretization procedures reduce a problem to one of a finite number of unknowns by dividing the solution region into elements and by expressing the unknown field variable in terms of assumed approximating functions within each element. The approximating functions are defined in terms of the values of the field variables at specified points called nodes or nodal points. The nodal values of the field variable and the interpolation functions for the elements completely define the behavior of the field variable within the elements. For the finite element representation of a problem, the nodal value of the field variable becomes new unknowns. Once the unknowns are found, the interpolation functions define the field variable throughout the assemblage of elements.

The set of functions used for approximation is generally a set of piecewise polynomials of fixed degree in  $x$  and  $y$ , and the approximation requires that the polynomials be pieced together in such a manner that the resulting function is continuous with an integrable or continuous first or second derivative on the entire region. Polynomials of linear type in  $x$  and  $y$ , i.e.,

$$\phi(x, y) = a + bx + cy,$$

are commonly used with triangular elements, while polynomials of bilinear type in  $x$  and  $y$ ,

$$\phi(x, y) = a + bx + cy + dxy,$$

are used with rectangular elements.

Suppose that the region  $\mathfrak{R}$  has been subdivided into triangular elements. The collection of triangles is denoted  $D$ . Then the linear test function can be expressed as

$$\phi(x, y) = \sum_{i=1}^m \gamma_i \phi_i(x, y)$$

where  $\phi_1, \phi_2, \dots, \phi_m$  are linearly independent piecewise linear polynomials, called basis functions, and  $\gamma_1, \gamma_2, \dots, \gamma_m$  are constants. Choice of basis functions is very important, since an appropriate choice can often make the matrix  $A$ , ( $A\mathbf{c} = \mathbf{b}$ ), positive definite and banded. Suppose a triangular element is made as Figure 4.1; then a linear basis function will be chosen as follows:

$$\varphi_p = L_p = \frac{1}{2S_\Delta} (a_p + b_p x + c_p y)$$

where  $a_p = x_q y_r - x_r y_q$ ,  $b_p = y_q - y_r$ ,  $c_p = x_r - x_q$ , and

$$S_\Delta = \frac{1}{2} [x_p (y_q - y_r) + x_q (y_r - y_p) + x_r (y_p - y_q)] = \text{the area of the triangle element.}$$

Now, a test function for  $T(x, y, z)$  can be used for approximation:

$$T_h(x, y, z) = \sum_{p=1}^N T_p(z) \varphi_p(x, y)$$

where  $N$  is the number of grid points in the  $x$ - $y$  cross-section.

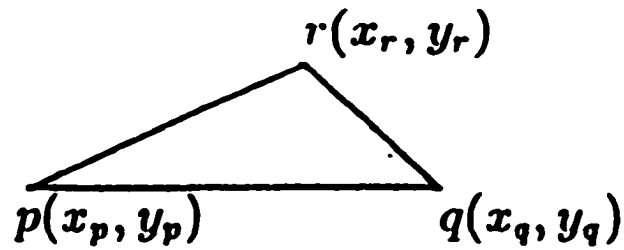


**Figure 4.1. A triangular element**

### **4.2. Finite Element-Finite Difference Scheme**

For convenience, we omit  $l$  and denote  $q_3$  as  $q$  in the governing equations (3.7) through (3.10). Now we first substitute Equation (3.9) into Equation (3.7). This gives

$$\rho C_p \frac{\partial T}{\partial t} = k \left( \frac{\partial^2 T}{\partial x^2} + \frac{\partial^2 T}{\partial y^2} \right) - \frac{\partial q}{\partial z} + Q \quad (4.1)$$

Equation (4.1) coupled with the equation

$$q + \tau_q \frac{\partial q}{\partial t} = -k \left[ \frac{\partial T}{\partial z} + \tau_r \frac{\partial}{\partial t} \left( \frac{\partial T}{\partial z} \right) \right] \quad (4.2)$$

are the governing equations for  $T$  and  $q$ .

Secondly, we multiply  $\varphi$  on both sides of Equation (4.1) and then integrate both sides of the equation over the domain  $\mathcal{H}$ . That gives

$$\iint_{\mathcal{H}} \rho C_p \frac{\partial T}{\partial t} \varphi dx dy = \iint_{\mathcal{H}} \left[ k \left( \frac{\partial^2 T}{\partial x^2} + \frac{\partial^2 T}{\partial y^2} \right) \varphi - \frac{\partial q}{\partial z} \varphi + Q \varphi \right] dx dy$$

where  $\varphi(x, y)$  is a basis function in the Sobolev space  $H^1$  and  $\mathcal{H}$  is the  $x$ - $y$  cross-section

of the thin film in the  $x$ - $y$  directions. Since we assume that  $\frac{\partial T}{\partial \bar{\nu}} = 0$  on the boundary of  $\mathcal{H}$

the above equation becomes, by the Green's formula,

$$\iint_{\mathcal{H}} \rho C_p \frac{\partial T}{\partial t} \varphi dx dy = \iint_{\mathcal{H}} [k(\frac{\partial T}{\partial x} \frac{\partial \varphi}{\partial x} + \frac{\partial T}{\partial y} \frac{\partial \varphi}{\partial y}) \varphi - \frac{\partial q}{\partial z} \varphi + Q \varphi] dx dy \quad (4.3)$$

We construct a finite element mesh in  $\mathcal{H}$  as shown in Figure 4.2, and write the test functions for  $T(x, y, z, t)$  and  $q(x, y, z, t)$  as follows:

$$T_h(x, y, z, t) = \sum_{p=1}^N T_p(z, t) \varphi_p(x, y), \quad q_h(x, y, z, t) = \sum_{p=1}^N q_p(z, t) \varphi_p(x, y),$$

where  $\varphi_p(x, y)$  is a basis function,  $N$  is the number of grid points in  $\mathcal{H}$ , and  $p$  is a nodal point.

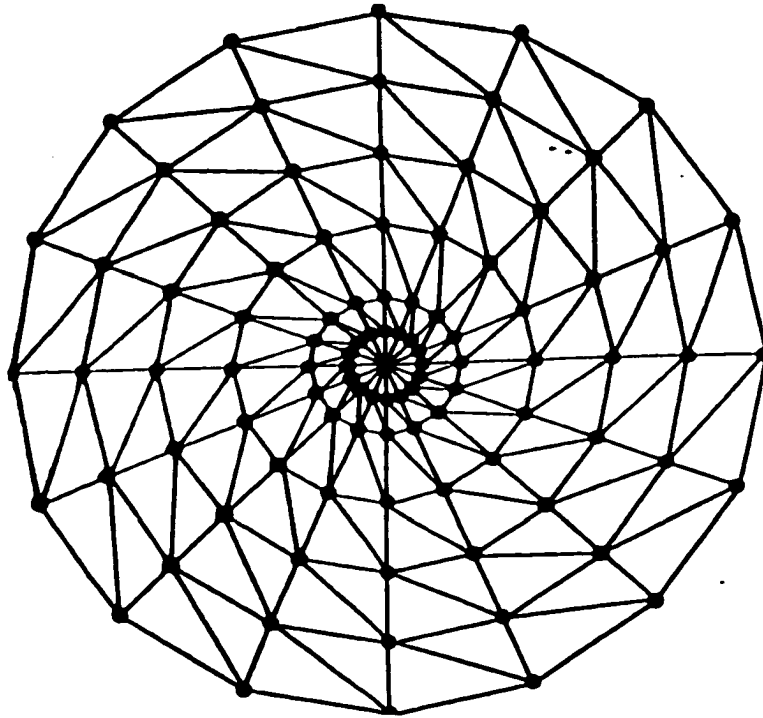


**Figure 4.2.** The finite element mesh in the  $x$ - $y$  cross-section.

Also, we let  $Q_h = \sum_{p=1}^N Q_p \varphi_p(x, y)$  as an interpolant of  $Q$ . Replacing  $T$ ,  $q$ ,  $Q$ , and  $\varphi$  in

Equation (4.3) by  $T_h, q_h, Q_h$ , and  $\varphi_q$ , respectively, we obtain

$$\begin{aligned} \sum_{p=1}^N \rho C_p \frac{\partial T_p}{\partial t} \iint_{\mathfrak{R}} \varphi_p \varphi_q dx dy = & \\ & - \sum_{p=1}^N k T_p \iint_{\mathfrak{R}} \left( \frac{\partial \varphi_p}{\partial x} \frac{\partial \varphi_q}{\partial x} + \frac{\partial \varphi_p}{\partial y} \frac{\partial \varphi_q}{\partial y} \right) dx dy \\ & - \sum_{p=1}^N \frac{\partial q_p}{\partial z} \iint_{\mathfrak{R}} \varphi_p \varphi_q dx dy \\ & + \sum_{p=1}^N Q_p \iint_{\mathfrak{R}} \varphi_p \varphi_q dx dy, \end{aligned} \quad q = 1, 2, \dots, N \quad (4.3)$$

Introducing the vector notations  $\bar{T}(z, t) = [T_1(z, t), \dots, T_N(z, t)]^T$ ,

$$\bar{q}(z, t) = (q_1, \dots, q_N)^T,$$

$$\bar{Q}(z, t) = (Q_1, \dots, Q_N)^T,$$

and the matrices  $M_{N \times N}$  and  $K_{N \times N}$  with the two respective entries,

$$m_{qp} = \iint_{\mathfrak{R}} \varphi_p \varphi_q dx dy$$

and

$$k_{qp} = \iint_{\mathfrak{R}} \left[ k \left( \frac{\partial \varphi_p}{\partial x} \frac{\partial \varphi_q}{\partial x} + \frac{\partial \varphi_p}{\partial y} \frac{\partial \varphi_q}{\partial y} \right) \right] dx dy$$

we can express the systems in Equations (4.2) and (4.3) into matrix forms as follows:

$$\rho C_p M \frac{\partial \bar{T}}{\partial t} = -k K \bar{T} - M \frac{\partial \bar{q}}{\partial z} + M \bar{Q} \quad (4.4)$$

and

$$\bar{q} + \tau_c \frac{\partial \bar{q}}{\partial t} = -k \left[ \frac{\partial \bar{T}}{\partial z} + \tau_T \frac{\partial}{\partial t} \left( \frac{\partial \bar{T}}{\partial z} \right) \right] \quad (4.5)$$

where  $M$  is the capacitance matrix and  $K$  is the conductance matrix. Both matrices are symmetric and positive definite. Also, they are sparse matrices. For simplification, we apply the lumped mass technique to obtain a diagonal matrix  $D_M$  and then replace  $M$  by  $D_M$  in Equation (4.4) to give

$$\rho C_p D_M \frac{\partial \bar{T}}{\partial t} = -k K \bar{T} - D_M \frac{\partial \bar{q}}{\partial z} + D_M \bar{Q} \quad (4.6)$$

where each entry  $d_p$  at the diagonal of  $D_M$  is  $\frac{1}{3} \sum_{\Delta} S_{\Delta}$  (i.e., one-third of the sum of all elements with node  $p$  as one vertex).

Now let's discretize the above Equations (4.5) and (4.6) using a finite-difference method. We first employ a mesh where it is a staggered grid in the  $z$  direction, as shown in Figure 4.3.

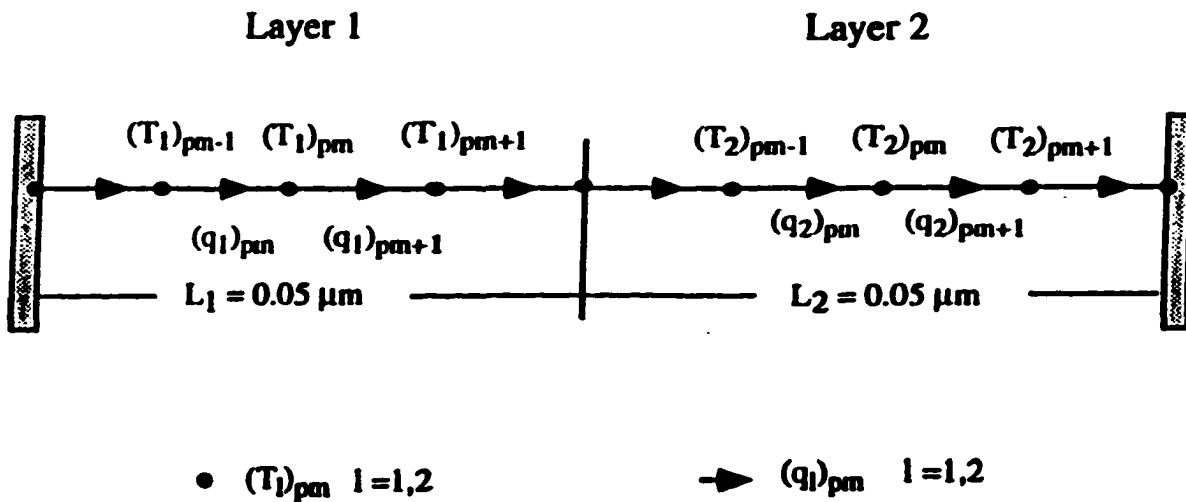


**Figure 4.3.** A staggered mesh in the  $z$  direction for a double-layered thin film.

Let  $\bar{T}_m^n$  denote  $\bar{T}(m\Delta z, n\Delta t)$ , where  $\Delta z$  and  $\Delta t$  are the  $z$  directional spatial and temporal mesh sizes, respectively,  $m = 0, 1, \dots, N_z + 1$ , while  $\bar{q}_m^n = (m\Delta z, n\Delta t)$ ,  $m = 0, 1, \dots, N_z + 1$ . Equation (4.5) and (4.6) are discretized using a Crank-Nicholson type of finite difference

$$\begin{aligned} \rho C_p D_M \frac{\bar{T}_m^{n+1} - \bar{T}_m^n}{\Delta t} = & -\frac{k}{2} K (\bar{T}_m^{n+1} + \bar{T}_m^n) \\ & -\frac{1}{2\Delta z} D_M (\bar{q}_{m+1}^{n+1} - \bar{q}_m^{n+1} + \bar{q}_{m+1}^n - \bar{q}_m^n) \\ & + D_M \bar{Q}_m^{n+\frac{1}{2}} \end{aligned} \quad (4.7)$$

$$\begin{aligned} \frac{1}{2} \bar{q}_m^{n+1} + \frac{1}{2} \bar{q}_m^n + \tau_q \frac{\bar{q}_m^{n+1} - \bar{q}_m^n}{\Delta t} = & -\frac{k}{\Delta z} \left\{ \frac{1}{2} (\bar{T}_m^{n+1} - \bar{T}_{m-1}^{n+1}) + \frac{1}{2} (\bar{T}_m^n - \bar{T}_{m-1}^n) \right. \\ & \left. + \frac{\tau_T}{\Delta t} [\bar{T}_m^{n+1} - \bar{T}_{m-1}^{n+1} - \bar{T}_m^n + \bar{T}_{m-1}^n] \right\}, \end{aligned} \quad (4.8)$$

where  $m = 1, \dots, N_z$ . Next, we simplify Equation (4.7) to obtain an equation for solving  $\bar{T}_m^{n+1}$ . To this end, we solve for  $\bar{q}_m^{n+1}$  from Equation (4.8) to obtain

$$\begin{aligned} \bar{q}_m^{n+1} = & \left( \frac{1}{2} + \frac{\tau_q}{\Delta t} \right)^{-1} \left( -\frac{1}{2} + \frac{\tau_q}{\Delta t} \right) \bar{q}_m^n \\ & - \left( \frac{1}{2} + \frac{\tau_q}{\Delta t} \right)^{-1} \frac{k}{\Delta z} \left\{ \left( \frac{1}{2} + \frac{\tau_T}{\Delta t} \right) (\bar{T}_m^{n+1} - \bar{T}_{m-1}^{n+1}) \right. \\ & \left. + \left( \frac{1}{2} - \frac{\tau_T}{\Delta t} \right) (\bar{T}_m^n - \bar{T}_{m-1}^n) \right\}. \end{aligned} \quad (4.9)$$

Substituting  $\bar{q}_m^{n+1}$  into Equation (4.7), we obtain

$$\begin{aligned}
\rho C_p D_M \frac{\bar{T}_m^{n+1} - \bar{T}_m^n}{\Delta t} &= -\frac{k}{2} K(\bar{T}_m^{n+1} + \bar{T}_m^n) \\
&+ \frac{k}{2\Delta z^2} \left(\frac{1}{2} + \frac{\tau_q}{\Delta t}\right)^{-1} \left(\frac{1}{2} + \frac{\tau_T}{\Delta t}\right) D_M (\bar{T}_{m+1}^{n+1} - 2\bar{T}_m^{n+1} + \bar{T}_{m-1}^{n+1}) \\
&+ \frac{k}{2\Delta z^2} \left(\frac{1}{2} + \frac{\tau_q}{\Delta t}\right)^{-1} \left(\frac{1}{2} - \frac{\tau_T}{\Delta t}\right) D_M (\bar{T}_{m+1}^n - 2\bar{T}_m^n + \bar{T}_{m-1}^n) \\
&- \frac{k}{2\Delta z} \left[1 + \left(\frac{1}{2} + \frac{\tau_q}{\Delta t}\right)^{-1} \left(-\frac{1}{2} + \frac{\tau_T}{\Delta t}\right)\right] D_M (\bar{q}_{m+1}^n - \bar{q}_m^n) + D_M \bar{Q}_m^{n+\frac{1}{2}} \quad (4.10)
\end{aligned}$$

Hence, solve  $\bar{T}_m^{n+1}$  from Equation (4.10) and then  $\bar{q}_m^{n+1}$  can be solved from Equation (4.9).

### 4.3. Preconditioned Richardson Iteration

Since Equation (4.10) is a three-dimensional implicit scheme, iterative techniques must be used. It will involve heavy computations, and simplification of the computation is desired. To do so, the preconditioned Richardson method will be employed. Equation (4.10) is solved using the following iteration:

$$\begin{aligned}
L_{pre}(\bar{T}_m^{n+1})^{(i+1)} &= L_{pre}(\bar{T}_m^{n+1})^{(i)} \\
&- \omega \left\{ D_M [(\bar{T}_m^{n+1})^{(i)} - \bar{T}_m^n] - \frac{k\Delta t}{2\rho C_p} K[(\bar{T}_m^{n+1})^{(i)} + \bar{T}_m^n] \right. \\
&- \frac{k\Delta t}{2\rho C_p \Delta z^2} \left(\frac{1}{2} + \frac{\tau_q}{\Delta t}\right)^{-1} \left(\frac{1}{2} + \frac{\tau_T}{\Delta t}\right) D_M [(\bar{T}_{m+1}^{n+1})^{(i)} - 2(\bar{T}_m^{n+1})^{(i)} + (\bar{T}_{m-1}^{n+1})^{(i)}] \\
&- \frac{k\Delta t}{2\rho C_p \Delta z^2} \left(\frac{1}{2} + \frac{\tau_q}{\Delta t}\right)^{-1} \left(\frac{1}{2} - \frac{\tau_T}{\Delta t}\right) D_M [\bar{T}_{m+1}^n - 2\bar{T}_m^n + \bar{T}_{m-1}^n] \\
&\left. + \frac{\Delta t}{2\rho C_p \Delta z} \left[1 + \left(\frac{1}{2} + \frac{\tau_q}{\Delta t}\right)^{-1} \left(-\frac{1}{2} + \frac{\tau_T}{\Delta t}\right)\right] D_M (\bar{q}_{m+1}^n - \bar{q}_m^n) - \frac{\Delta t}{\rho C_p} D_M \bar{Q}_m^{n+\frac{1}{2}} \right\}
\end{aligned}$$

$$i = 0, 1, 2, \dots, \quad (4.11)$$

where

$$L_{pre} = D_M + \frac{k\Delta t}{2\rho C_p} 2D_K - \frac{k}{2\rho C_p \Delta z^2} \left(\frac{1}{2} + \frac{\tau_q}{\Delta t}\right)^{-1} \left(\frac{1}{2} + \frac{\tau_T}{\Delta t}\right) D_M \delta_z^2 \quad (4.12)$$

is the preconditioner,  $\omega$  is a relaxation parameter,  $0 \leq \omega \leq 1$ ,  $D_K$  is a diagonal matrix where each diagonal entry of  $D_K$  is chosen to be the sum of absolute values of elements in

each row of  $K$ .  $\delta_z^2$  is a difference operator such that  $\delta_z^2 \bar{T}_m^n = \bar{T}_{m+1}^n - 2\bar{T}_m^n + \bar{T}_{m-1}^n$ .

Introducing  $\bar{T}^n = [\bar{T}_1^n, \bar{T}_2^n, \dots, \bar{T}_{N_i}^n]^T$ ,

$$M = \begin{bmatrix} M & & & \\ & M & & \\ & & \ddots & \\ & & & M \end{bmatrix}, \quad K = \begin{bmatrix} K & & & \\ & K & & \\ & & \ddots & \\ & & & K \end{bmatrix},$$

$$D_M = \begin{bmatrix} D_M & & & \\ & D_M & & \\ & & \ddots & \\ & & & D_M \end{bmatrix}, \quad D_K = \begin{bmatrix} D_K & & & \\ & D_K & & \\ & & \ddots & \\ & & & D_K \end{bmatrix},$$

$$C_M = \begin{bmatrix} 2M & -M & & & \\ -M & 2M & -M & & \\ & & \ddots & \ddots & \ddots \\ & & & -M & 2M & -M \\ & & & & -M & 2M \end{bmatrix}, \quad \dots$$

$$C_{D_M} = \begin{bmatrix} 2D_M & -D_M & & & \\ -D_M & 2D_M & -D_M & & \\ & & \ddots & \ddots & \ddots \\ & & & -D_M & 2D_M & -D_M \\ & & & & -D_M & 2D_M \end{bmatrix},$$

We rewrite Equation (4.11) into a vector form:

$$L_{pre}(\bar{T}^{n+1})^{(i+1)} = L_{pre}(\bar{T}^{n+1})^{(i)} - \omega \left\{ M(\bar{T}^{n+1})^{(i)} + \frac{k\Delta t}{2\rho C_p} K(\bar{T}^{n+1})^{(i)} + \frac{k\Delta t}{2\rho C_p \Delta z^2} \left( \frac{1}{2} + \frac{\tau_q}{\Delta t} \right)^{-1} \left( \frac{1}{2} + \frac{\tau_T}{\Delta t} \right) C_M(\bar{T}^{n+1})^{(i)} + \bar{d} \right\} \quad (4.13)$$

where the preconditioner is chosen as follows:

$$L_{pre} = D_M + \frac{k\Delta t}{2\rho C_p} D_K + \frac{k\Delta t}{2\rho C_p \Delta z^2} \left( \frac{1}{2} + \frac{\tau_q}{\Delta t} \right)^{-1} \left( \frac{1}{2} + \frac{\tau_T}{\Delta t} \right) C_{D_M}, \quad (4.14)$$

It is well known from the numerical linear algebra that the iteration process converges if the iteration operator

$$R \equiv I - \omega L_{pre}^{-1} \left[ D_M + \frac{k\Delta t}{2\rho C_p} K + \frac{k\Delta t}{2\rho C_p \Delta z^2} \left( \frac{1}{2} + \frac{\tau_q}{\Delta t} \right)^{-1} \left( \frac{1}{2} + \frac{\tau_T}{\Delta t} \right) C_{D_M} \right] \quad (4.15)$$

has a spectral radius  $\rho(R) < 1$ . Let  $\xi$  be the eigenvalue of

$$L_{pre}^{-1} \left[ D_M + \frac{k\Delta t}{\rho C_p} K + \frac{k\Delta t}{\rho C_p \Delta z^2} \left( \frac{1}{2} + \frac{\tau_q}{\Delta t} \right)^{-1} \left( \frac{1}{2} + \frac{\tau_T}{\Delta t} \right) C_{D_M} \right]$$

and  $\bar{x}$  be the eigenvector. Then, we have the expression below:

$$\xi = \frac{\bar{x}^T D_M \bar{x} + \frac{k\Delta t}{\rho C_p} \bar{x}^T K \bar{x} + \frac{k\Delta t}{\rho C_p \Delta z^2} \left( \frac{1}{2} + \frac{\tau_q}{\Delta t} \right)^{-1} \left( \frac{1}{2} + \frac{\tau_T}{\Delta t} \right) \bar{x}^T C_{D_M} \bar{x}}{\bar{x}^T D_M \bar{x} + \frac{k\Delta t}{\rho C_p} \bar{x}^T D_K \bar{x} + \frac{k\Delta t}{\rho C_p \Delta z^2} \left( \frac{1}{2} + \frac{\tau_q}{\Delta t} \right)^{-1} \left( \frac{1}{2} + \frac{\tau_T}{\Delta t} \right) \bar{x}^T C_{D_M} \bar{x}} \quad (4.16)$$

To show that  $0 < \xi < 1$ , it is sufficient to show that  $\bar{x}^T D_K \bar{x} \geq \bar{x}^T K \bar{x}$ . To show  $\bar{x}^T D_K \bar{x} \geq \bar{x}^T K \bar{x}$ , it is sufficient to show that  $D_K - K$  is positive definite. Since the

elements of  $D_K - K$  satisfies  $dk_{pp} \geq \sum_{\substack{q=1 \\ q \neq p}}^N |dk_{qq}|$  and  $K$  is a sparse matrix,  $D_K - K$  is

symmetric, irreducible, and diagonally dominant. By the theory of numerical linear algebra,  $D_K - K$  is positive definite. Hence, we have  $\bar{x}^T D_K \bar{x} \geq \bar{x}^T K \bar{x}$ . Therefore, we conclude that  $0 < \xi < 1$ . If one chooses the relaxation parameter to be equal to 1, i.e.,  $\omega = 1$ , then spectral radius  $\rho(R)$  will be less than 1. Hence, this iterative method will be convergent. It should be noted that, in the preconditioning method, the original system will change to be a block tri-diagonal system. Only a block tri-diagonal linear system is solved for each iteration in Equation (4.13). The Gaussian elimination method can be applied for solving this system. It will significantly reduce the computation.

#### 4.4. A Domain Decomposition Algorithm

We now apply the preconditioned Richardson iteration (4.11) to both layers ( $l = 1, 2$ ) as follows:

$$\begin{aligned}
L_{pre}^{(l)} [(\bar{T}^{(l)})_m^{n+1}]^{(i+1)} = & \\
L_{pre}^{(l)} [(\bar{T}^{(l)})_m^{n+1}]^{(i)} - \omega \{ D_M [(\bar{T}^{(l)})_m^{n+1}]^{(i)} - (\bar{T}^{(l)})_m^n - \frac{k^{(l)} \Delta f}{2 \rho^{(l)} C_p^{(l)}} K [(\bar{T}^{(l)})_m^{n+1}]^{(i)} + (\bar{T}^{(l)})_m^n \} & \\
- \frac{k^{(l)} \Delta f}{2 \rho^{(l)} C_p^{(l)} \Delta z^2} \left( \frac{1}{2} + \frac{\tau_q}{\Delta f} \right)^{-1} \left( \frac{1}{2} + \frac{\tau_T}{\Delta f} \right) D_M [(\bar{T}^{(l)})_{m+1}^{n+1}]^{(i)} - 2 [(\bar{T}^{(l)})_m^{n+1}]^{(i)} + [(\bar{T}^{(l)})_{m-1}^{n+1}]^{(i)} & \\
- \frac{k^{(l)} \Delta f}{2 \rho^{(l)} C_p^{(l)} \Delta z^2} \left( \frac{1}{2} + \frac{\tau_q}{\Delta f} \right)^{-1} \left( \frac{1}{2} - \frac{\tau_T}{\Delta f} \right) D_M [(\bar{T}^{(l)})_{m+1}^n - 2(\bar{T}^{(l)})_m^n + (\bar{T}^{(l)})_{m-1}^n] & \\
+ \frac{\Delta f}{2 \rho^{(l)} C_p^{(l)} \Delta z} \left[ 1 + \left( \frac{1}{2} + \frac{\tau_q}{\Delta f} \right)^{-1} \left( -\frac{1}{2} + \frac{\tau_T}{\Delta f} \right) \right] D_M [(\bar{q}^{(l)})_{m+1}^n - (\bar{q}^{(l)})_m^n] - \frac{\Delta f}{\rho^{(l)} C_p^{(l)}} D_M \bar{Q}_m^{n+\frac{1}{2}} \} & \\
i = 0, 1, 2, \dots & \quad (4.17)
\end{aligned}$$

where the preconditioner is chosen as follows:

$$L_{pre}^{(i)} = 2D_M + \frac{k^{(i)}\Delta t}{2\rho^{(i)}C_p^{(i)}}2D_K - \frac{k^{(i)}\Delta t}{2\rho^{(i)}C_p^{(i)}\Delta z^2}\left(\frac{1}{2} + \frac{\tau_q^{(i)}}{\Delta t}\right)^{-1}\left(\frac{1}{2} + \frac{\tau_T^{(i)}}{\Delta t}\right)D_M\delta_z^2 \quad (4.18)$$

At the interface, we assume that

$$[(T^{(1)})_{\rho N_i+1}^{n+1}]^{(i+1)} = [(T^{(2)})_{\rho 0}^{n+1}]^{(i+1)} \quad (4.19)$$

and the temperature gradients are the same, i.e.,

$$k^{(1)}\{[(T^{(1)})_{\rho N_i+1}^{n+1}]^{(i+1)} - [(T^{(1)})_{\rho N_i}^{n+1}]^{(i+1)}\} = k^{(2)}\{[(T^{(2)})_{\rho 1}^{n+1}]^{(i+1)} - [(T^{(2)})_{\rho 0}^{n+1}]^{(i+1)}\} \quad (4.20)$$

On the top and bottom surfaces, we assume that

$$(T^{(1)})_{\rho 0}^{n+1} = (T^{(2)})_{\rho 1}^{n+1} \quad \text{and} \quad (T^{(2)})_{\rho N_i+1}^{n+1} = (T^{(2)})_{\rho N_i}^{n+1}$$

These assumptions are based on that no heat is lost on these surfaces during the transient response because the use of an ultrafast pulsed laser source is assumed. Once  $(T^{(i)})_{\rho m}^{n+1}$  is obtained, we can solve  $(\bar{q}^{(i)})_{\rho m}^{n+1}$  from Equation (4.9). This gives

$$\begin{aligned} (\bar{q}^{(i)})_m^{n+1} &= \left(\frac{1}{2} + \frac{\tau_q^{(i)}}{\Delta t}\right)^{-1} \left(-\frac{1}{2} + \frac{\tau_T^{(i)}}{\Delta t}\right) (\bar{q}^{(i)})_m^n \\ &\quad - \left(\frac{1}{2} + \frac{\tau_q^{(i)}}{\Delta t}\right)^{-1} \frac{k^{(i)}}{\Delta z} \left\{ \left(\frac{1}{2} + \frac{\tau_T^{(i)}}{\Delta t}\right) ((\bar{T}^{(i)})_m^{n+1} - (\bar{T}^{(i)})_{m-1}^{n+1}) \right. \\ &\quad \left. + \left(\frac{1}{2} - \frac{\tau_T^{(i)}}{\Delta t}\right) (\bar{T}_m^n - \bar{T}_{m-1}^n) \right\}. \end{aligned} \quad (4.21)$$

Equation (4.17) can be expressed into two tri-diagonal linear systems as follows:

$$\begin{aligned} -B_m^{(1)}[(\bar{T}^{(1)})_{m-1}^{n+1}]^{(i+1)} + A_m^{(1)}[(\bar{T}^{(1)})_m^{n+1}]^{(i+1)} - C_m^{(1)}[(\bar{T}^{(1)})_{m+1}^{n+1}]^{(i+1)} &= \bar{d}_m^{(1)}, \\ m &= 1, 2, \dots, N_z \end{aligned} \quad (4.22)$$

$$\begin{aligned} -B_m^{(2)}[(\bar{T}^{(2)})_{m-1}^{n+1}]^{(i+1)} + A_m^{(2)}[(\bar{T}^{(2)})_m^{n+1}]^{(i+1)} - C_m^{(2)}[(\bar{T}^{(2)})_{m+1}^{n+1}]^{(i+1)} &= \bar{d}_m^{(2)}, \\ m &= 1, 2, \dots, N_z \end{aligned} \quad (4.23)$$

where the matrices  $A_m^{(l)}$ ,  $B_m^{(l)}$ , and  $C_m^{(l)}$  are diagonal matrices. Since  $\{[(\bar{T}^{(l)})_m^{n+1}]^{(i+1)}\}$  ( $l = 1, 2$ ) are unknown at the interface between layers, the above two block tri-diagonal linear systems cannot be solved. To overcome this difficulty, we apply a parallel Gaussian elimination procedure to solve these two block tri-diagonal linear systems and hence develop a domain decomposition algorithm for thermal analysis of the double-layered thin film as follows:

**Step 1. Calculate the sequences  $\{\alpha_m^{(1)}, \beta_m^{(1)}\}$  and  $\{\alpha_m^{(2)}, \beta_m^{(2)}\}$  from Equations (4.12) and (4.13) as follows:**

$$\alpha_m^{(1)} = [A_m^{(1)} - B_m^{(1)}\alpha_{m-1}^{(1)}]^{-1}C_m^{(1)}, \quad \alpha_0^{(1)} = 0$$

$$\bar{\beta}_m^{(1)} = [A_m^{(1)} - B_m^{(1)}\alpha_{m-1}^{(1)}]^{-1}(\bar{d}_m^{(1)} + B_m^{(1)}\bar{\beta}_{m-1}^{(1)}), \quad \bar{\beta}_0^{(1)} = 0, \quad m = 0, 1, \dots, N_2$$

and

$$\alpha_m^{(2)} = [A_m^{(2)} - B_m^{(2)}\alpha_{m-1}^{(2)}]^{-1}C_m^{(2)}, \quad \alpha_{N_2+1}^{(2)} = 0$$

$$\bar{\beta}_m^{(2)} = [A_m^{(2)} - B_m^{(2)}\alpha_{m-1}^{(2)}]^{-1}(\bar{d}_m^{(2)} + B_m^{(2)}\bar{\beta}_{m-1}^{(2)}), \quad \bar{\beta}_{N_2+1}^{(2)} = 0, \quad m = N_2, \dots, 1$$

**Step 2. Substitute**

$$[(\bar{T}^{(1)})_{N_2}^{n+1}]^{(i+1)} = \alpha_{N_2}^{(1)}[(\bar{T}^{(1)})_{N_2+1}^{n+1}]^{(i+1)} + \bar{\beta}_{N_2}^{(1)}$$

and

$$[(\bar{T}^{(2)})_1^{n+1}]^{(i+1)} = \alpha_1^{(2)}[(\bar{T}^{(2)})_0^{n+1}]^{(i+1)} + \bar{\beta}_1^{(2)}$$

into the interfacial equation (4.20) to solve  $[(\bar{T}^{(1)})_{N_2+1}^{n+1}]^{(i+1)}$  and  $[(\bar{T}^{(2)})_0^{n+1}]^{(i+1)}$ .

**Step 3. Solve for the rest of the unknowns in  $\{[(\bar{T}^{(l)})_m^{n+1}]^{(i+1)}\}$  ( $l = 1, 2$ ) using**

$$[(\bar{T}^{(l)})_m^{n+1}]^{(i+1)} = \alpha_m^{(l)}[(\bar{T}^{(l)})_{m+1}^{n+1}]^{(i+1)} + \bar{\beta}_m^{(l)} \quad m = N_2, \dots, 1$$

and

$$[(\bar{T}^{(2)})_i^{n+1}]^{(i+1)} = \alpha_i^{(2)}[(\bar{T}^{(2)})_0^{n+1}]^{(i+1)} + \bar{\beta}_i^{(2)} \quad m = 1, \dots, N_2$$

The above iteration is continued with respect to  $i$  until a criterion for convergence is satisfied.

**Step 4. Solve  $\{[(\bar{q}^{(l)})_m^{n+1}]^{(i+1)}\}$  ( $l = 1, 2$ ) using Equation (4.21).**

It should be pointed out that in Step 1 we need to compute a number of matrix inverses. However, this is rather simple since we are dealing with diagonal matrices only.

## CHAPTER 5

### NUMERICAL RESULTS

To demonstrate the applicability of the numerical procedure, we investigate the temperature rise in a double-layered thin film with a gold surface layer and a chromium padding layer. The geometrical shape is a cylinder. The thicknesses of the gold layer and of the chromium padding layer are  $0.95\mu\text{m}$  each, while the radius in the x-y directions is 1 mm, as shown in Figure 5.1. The parameters of the properties of gold and chromium used in this analysis are listed in Table 5.1.

The heat source for both layers was chosen to be

$$Q(x, y, z, t) = 0.94J \left[ \frac{1-R}{t_p \delta} \right] e^{-\frac{z}{\delta} - a \frac{|t-2t_p|}{t_p}} \quad (5.1)$$

where  $J = 13.7 \frac{J}{m^2}$ ,  $t_p = 100 \text{ fs}$ ,  $\delta = 15.3 \text{ nm}$ ,  $R = 0.93$ .

The initial conditions were chosen as follows:

$$T^{(l)}(x, y, z, 0) = T_\infty \text{ and } \frac{\partial T^{(l)}}{\partial t}(x, y, z, 0) = 0$$

$$q_3^{(l)}(x, y, z, 0) = -\delta Q(x, y, z, 0), \quad l = 1, 2 \quad (5.2)$$

where  $T_\infty = 300K$ . Here, the initial conditions were chosen as the arguments in Section 3.3.

The boundary conditions are assumed to be  $q_3^{(1)} = 0$  on the top surface,  $q_3^{(2)} = 0$  on the bottom surface, and  $\bar{q} = 0$  on the lateral walls. Such boundary conditions arise from the case

that the double-layered thin film is subjected to a short-pulse laser irradiation. Hence, one may assume that no heat is lost from the surfaces of the film in the transient response.

To apply our numerical method, we chose a finite element mesh with the same 97 nodes in the x-y direction, as shown in Figure 5.2, for each layer, and chose 100 grid points in the z direction for gold and chromium layers, respectively. The basis function in the finite element approximation was chosen to be the linear function.

To use the preconditioned Richardson iteration (Equation (4.17)), we chose  $\omega = 1.0$ , and the convergent solutions  $\{(\bar{T}^{(l)})_m^{n+1}\} (l = 1, 2)$  were obtained until the criterion

$$\max \left| [(\bar{T}^{(l)})_m^{n+1}]^{(i+1)} - [(\bar{T}^{(l)})_m^{n+1}]^{(i)} \right| < 0.001 \quad (5.3)$$

was satisfied.

The numerical results were compared with those obtained using a finite difference method for a rectangular gold layer on a rectangular chromium padding layer by Dai and Nassar et al. (2000). That is,

$$\begin{aligned} L_{pre}^{(l)} [(\bar{T}^{(l)})_{jkm}^{n+1}]^{(i+1)} = & \\ L_{pre}^{(l)} [(\bar{T}^{(l)})_{jkm}^{n+1}]^{(i)} - \omega \left\{ \frac{[(T^{(l)})_{jkm}^{n+1}]^{(i)} - T_{jkm}^n}{\Delta t} - \frac{k^{(l)}}{2\rho^{(l)}C_p^{(l)}} (\delta_x^2 + \delta_y^2) ([ (T^{(l)})_{jkm}^{n+1} ]^{(i)} - (T^{(l)})_{jkm}^n ) \right. & \\ + \frac{k^{(l)}}{2\rho^{(l)}C_p^{(l)}\Delta z^2} \left( \frac{1}{2} + \frac{\tau_q^{(l)}}{\Delta t} \right)^{-1} \left( \frac{1}{2} + \frac{\tau_T^{(l)}}{\Delta t} \right) [ (T^{(l)})_{jkm+1}^n ]^{(i)} - 2 [ (T^{(l)})_{jkm}^{n+1} ]^{(i)} + [ (T^{(l)})_{jkm-1}^{n+1} ]^{(i)} & \\ - \frac{k^{(l)}}{2\rho^{(l)}C_p^{(l)}\Delta z^2} \left( \frac{1}{2} + \frac{\tau_q^{(l)}}{\Delta t} \right)^{-1} \left( \frac{1}{2} - \frac{\tau_T^{(l)}}{\Delta t} \right) [ (T^{(l)})_{jkm+1}^n - 2(T^{(l)})_{jkm}^n + (T^{(l)})_{jkm-1}^n ] & \\ + \frac{1}{2\rho^{(l)}C_p^{(l)}\Delta z} \left[ 1 + \left( \frac{1}{2} + \frac{\tau_q^{(l)}}{\Delta t} \right)^{-1} \left( \frac{1}{2} + \frac{\tau_T^{(l)}}{\Delta t} \right) \right] [ (q^{(l)})_{jkm}^n - (q^{(l)})_{jkm-1}^n ] - \frac{1}{\rho^{(l)}C_p^{(l)}} Q_{jkm}^{n+\frac{1}{2}} \Big\}, & \end{aligned}$$

$$l = 1, 2, \quad i = 0, 1, 2, \dots \quad (5.4)$$

where

$$L_{pre}^{(l)} = 1 + 2 \left( \frac{k^{(l)} \Delta t}{\rho^{(l)} C_p^{(l)} \Delta x^2} + \frac{k^{(l)} \Delta t}{\rho^{(l)} C_p^{(l)} \Delta y^2} \right) - \frac{k^{(l)}}{2 \rho^{(l)} C_p^{(l)}} \left( \frac{1}{2} + \frac{\tau_q^{(l)}}{\Delta t} \right)^{-1} \left( \frac{1}{2} + \frac{\tau_r^{(l)}}{\Delta t} \right) \delta_z^2 \quad (5.5)$$

and

$$\begin{aligned} (q^{(l)})_{jkm}^{n+1} &= \left( \frac{1}{2} + \frac{\tau_q^{(l)}}{\Delta t} \right)^{-1} \left( -\frac{1}{2} + \frac{\tau_q^{(l)}}{\Delta t} \right) (q^{(l)})_{jkm}^n \\ &\quad - \left( \frac{1}{2} + \frac{\tau_r^{(l)}}{\Delta t} \right)^{-1} \left( -\frac{k^{(l)}}{\Delta z} \left\{ \left( \frac{1}{2} + \frac{\tau_r^{(l)}}{\Delta t} \right) [(T^{(l)})_{jkm}^{n+1} - (T^{(l)})_{jkm-1}^{n+1}] \right. \right. \\ &\quad \left. \left. + \left( \frac{1}{2} - \frac{\tau_r^{(l)}}{\Delta t} \right) [(T^{(l)})_{jkm}^n - (T^{(l)})_{jkm-1}^n] \right\} \right), \quad l = 1, 2, \quad (5.6) \end{aligned}$$

Figure 5.3 gives the temperature rises along the z axis for time  $t = 0.2$  ps, 0.25 ps, and 0.5 ps. Results were obtained using a time increment of 0.005 ps. These results were in good agreement with those obtained by Dai and Nassar et al. (2000).

Figure 5.4 shows the temperature change  $\left( \frac{\Delta T_1}{(\Delta T_1)_{max}} \right)$  on the surface of the gold layer.

The maximum temperature rise of  $T_1$  on the surface of the gold layer is about 10.98 K obtained by Dai and Nassar. The numerical results show a good agreement.

Figures 5.5, 5.6, and 5.7 represented the contours of the temperature distribution in the r-z cross-section for time  $t = 0.2$  ps, 0.25 ps, and 0.5 ps.

To see the direction of the heat transfer, we chose the incident heat source being at the center area with a radius of 0.2 mm, one-fifth of the radius of the surface circle, as shown in Figure 5.8, while the temperature was fixed on the lateral walls. With the same numerical conditions, Figure 5.9 gives the temperature rise along the z axis for time  $t = 0.2$  ps, 0.25 ps,

and 0.5 ps. Results were obtained using a time increment of 0.005 ps. These results were again in good agreement with the previous work by Dai and Nassar. Figure 5.10 showed the temperature change  $\left(\frac{\Delta T_1}{(\Delta T_1)_{\max}}\right)$  at the center of the surface of the gold layer. Again, they were in good agreement.

Figures 5.11, 5.12, and 5.13 present the contours of the temperature distribution in the r-z cross section for time  $t = 0.2$  ps, 0.25 ps, and 0.5 ps. It can be seen that most of the heat is transferred from the gold layer to the chromium padding layer.

Furthermore, the preconditioned Richardson iteration is fast because the solution converges at most after a couple of iterations for each time step.

The above numerical results show that the method is accurate and efficient. The CPU time is about 90 seconds in a SGI Origin-2000 for  $t = 0.2$  ps and  $n = 40$ .

**Table 5.1. Properties of Gold and Chromium.**

<b>Property</b>	<b>Gold</b>	<b>Chromium</b>
<b><math>\rho, \text{Kg/m}^3</math></b>	<b>19300</b>	<b>7160</b>
<b><math>k, \text{W/m/K}</math></b>	<b>317</b>	<b>93</b>
<b><math>C_p, \text{kJ/kg/K}</math></b>	<b>129</b>	<b>449</b>
<b><math>\tau_q, \text{ps}</math></b>	<b>8.5</b>	<b>0.136</b>
<b><math>\tau_T, \text{ps}</math></b>	<b>90</b>	<b>7.86</b>

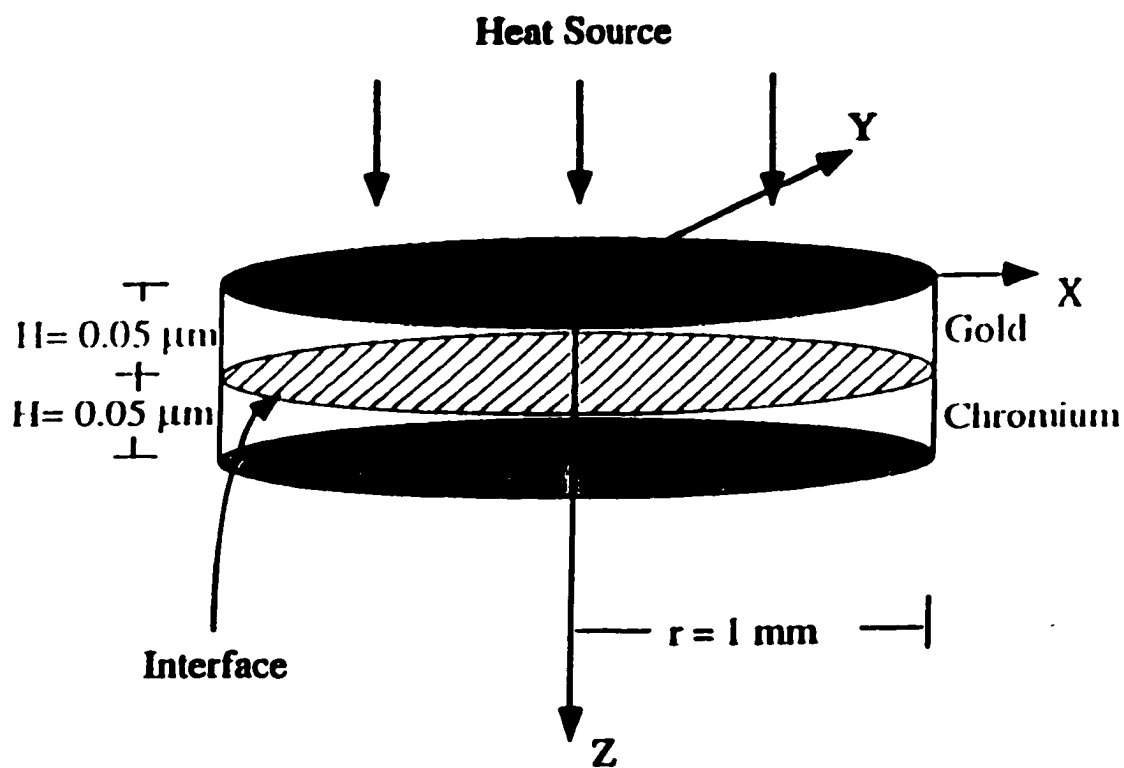


**Figure 5.1.** 3-D configuration of a double-layered cylindrical thin film.

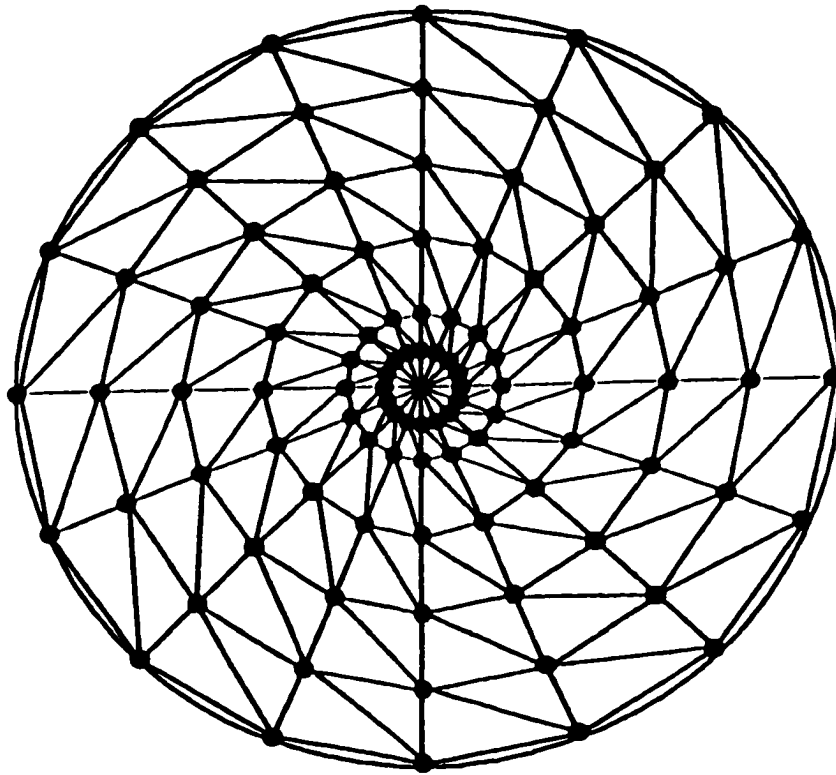


**Figure 5.2.** The finite element mesh in the x-y cross-section.

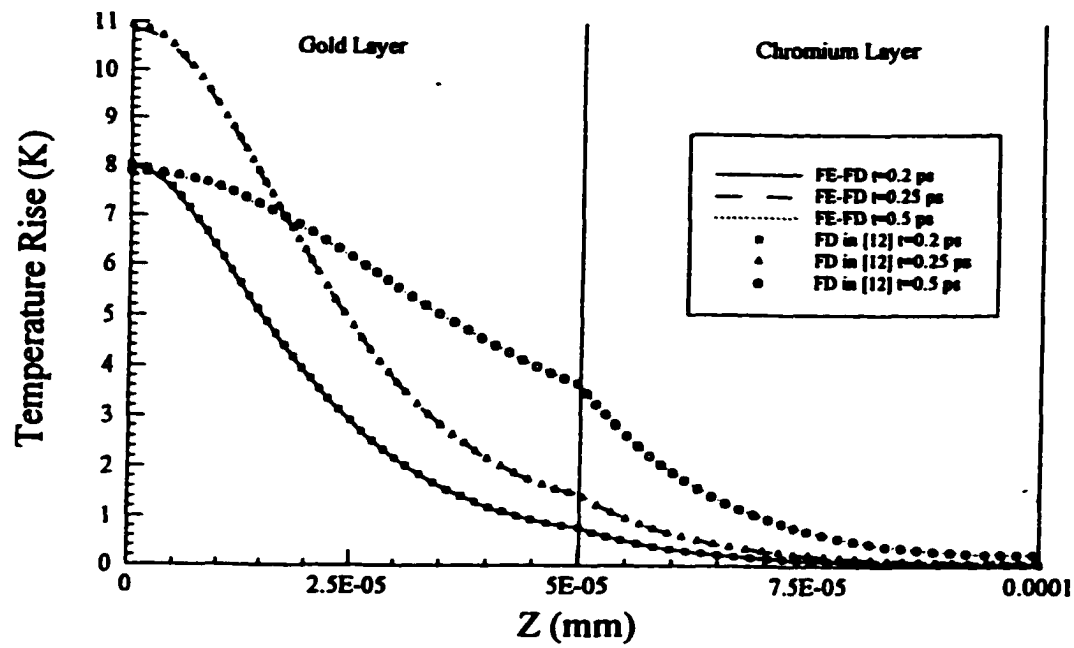


**Figure 5.3.** Temperature profiles along the z direction.

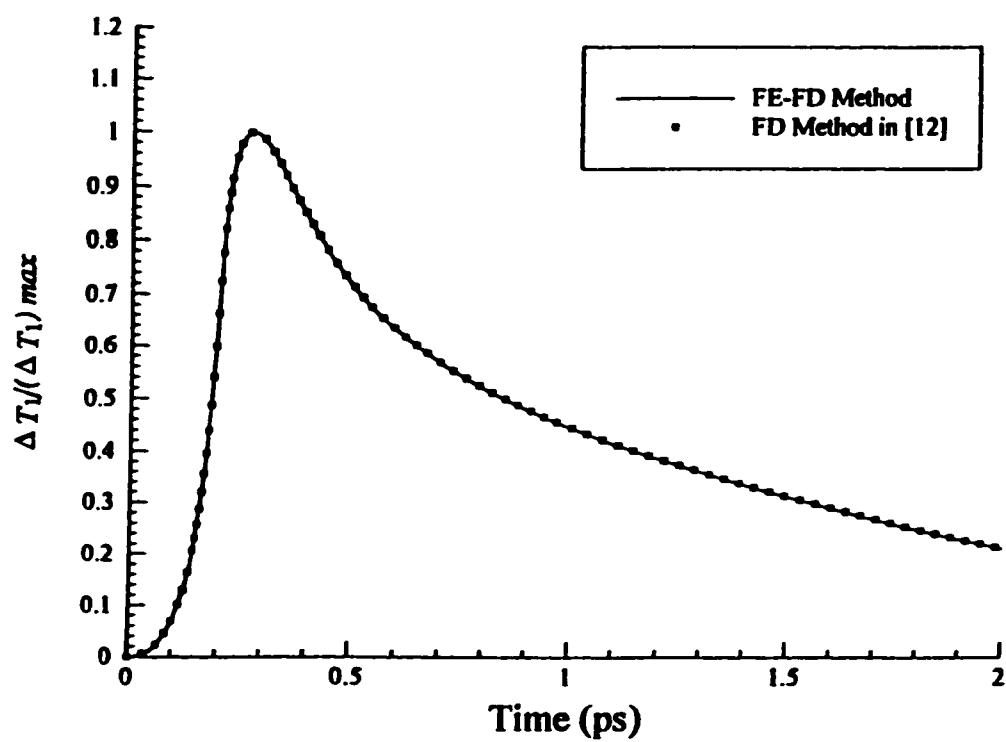


**Figure 5.4.** Temperature change on the surface of the gold layer.

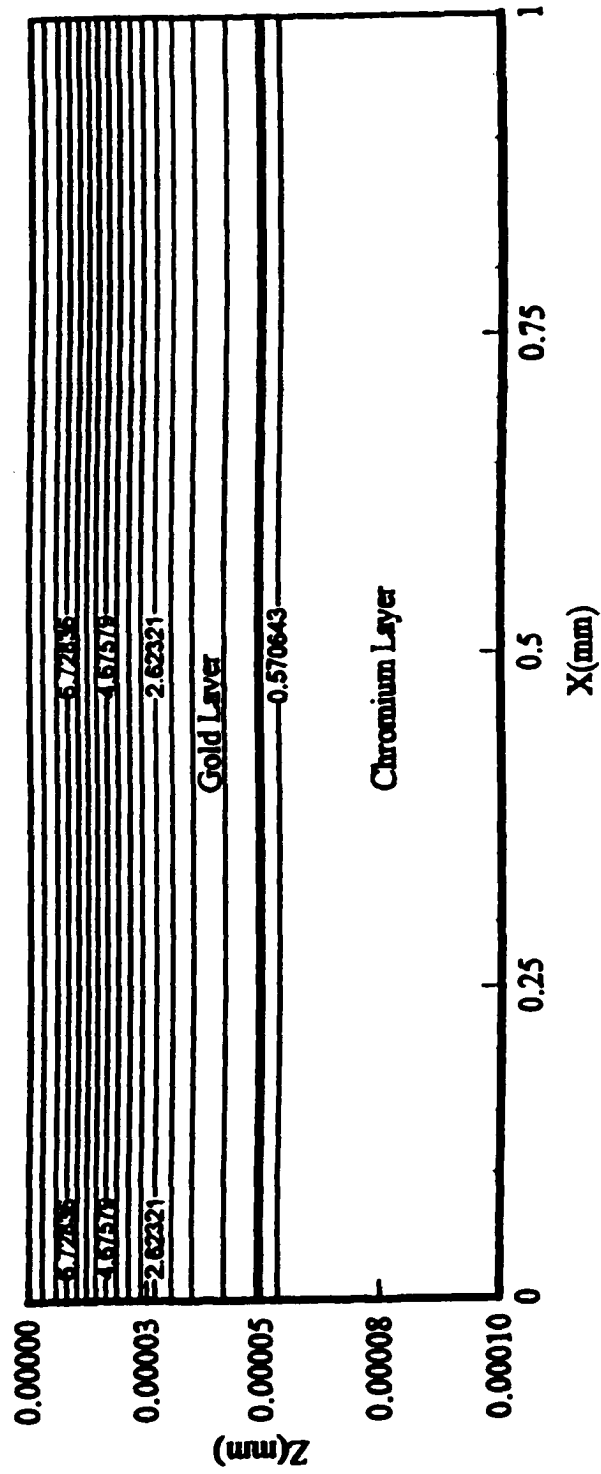


Figure 5.5. Contours of the temperature distribution in the x-z directions ( $t = 0.2$  ps).

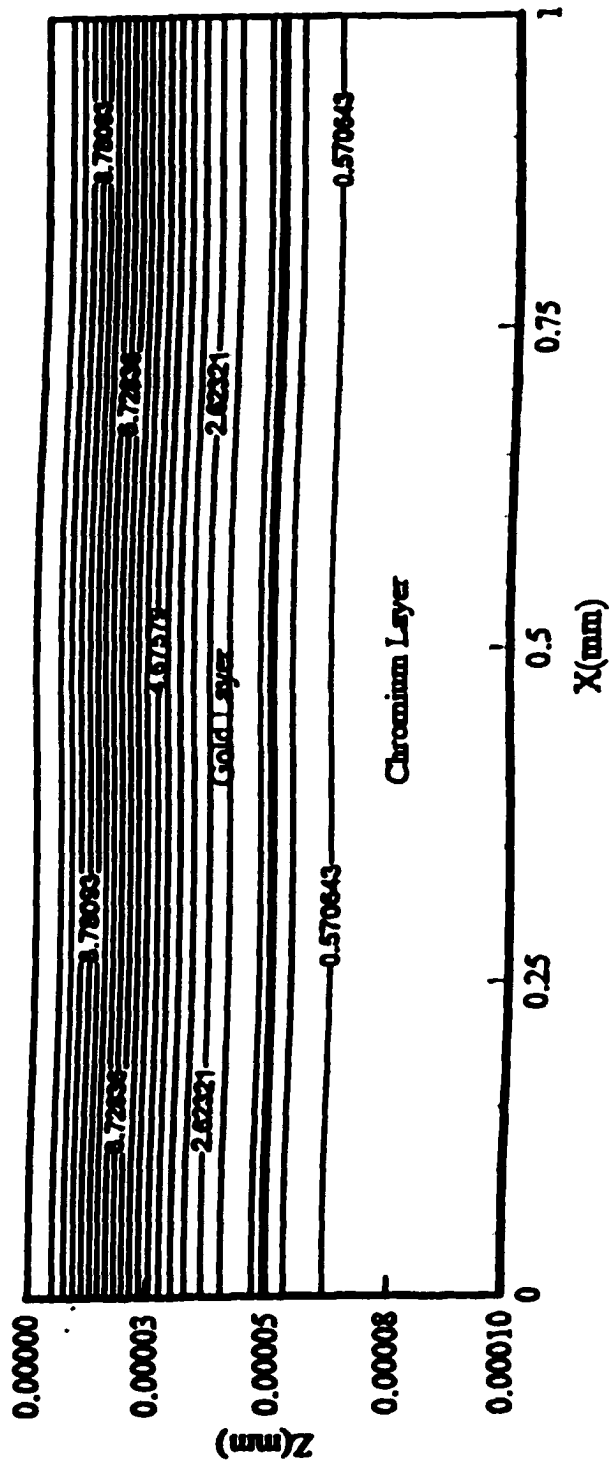


Figure 5.6. Contours of the temperature distribution in the x-z directions ( $t = 0.25$  ps).

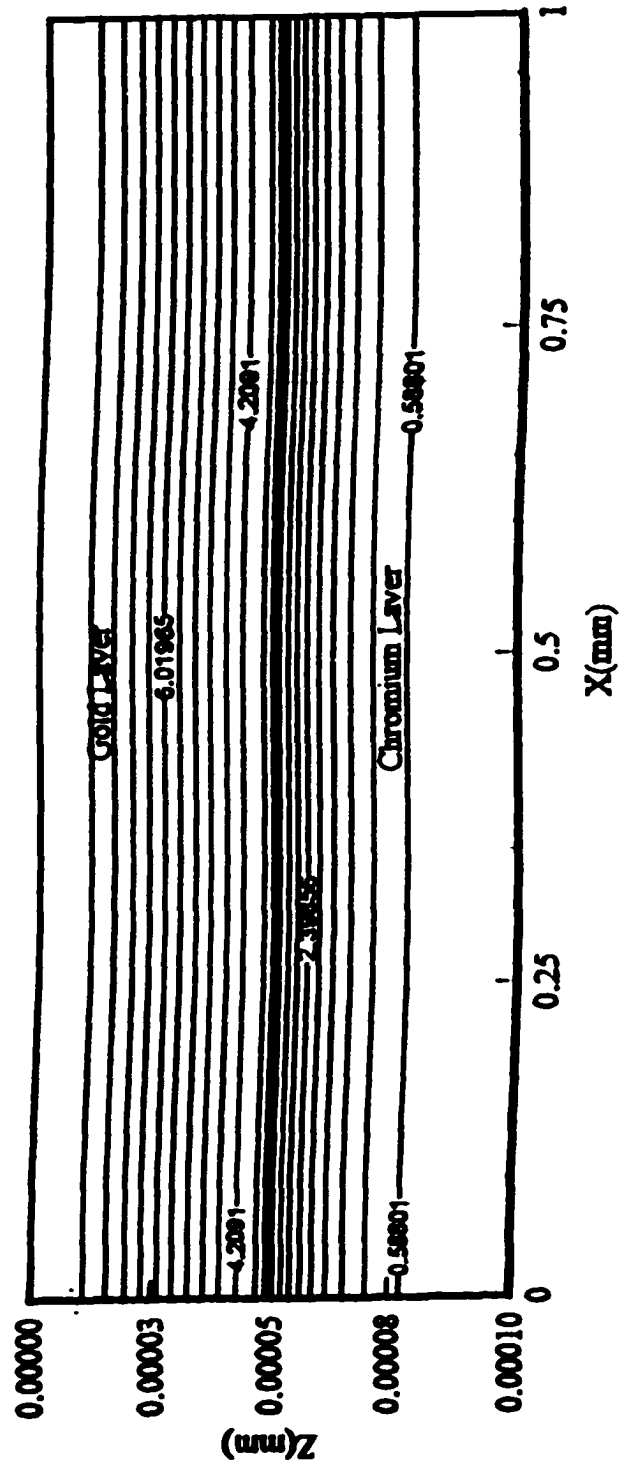
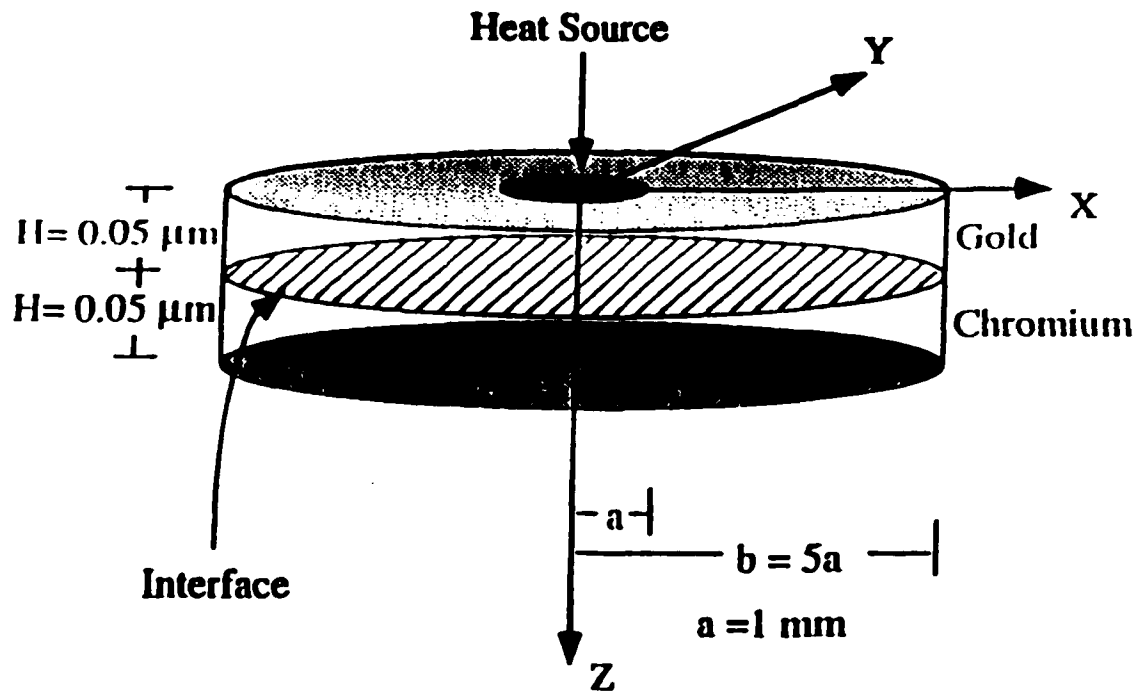
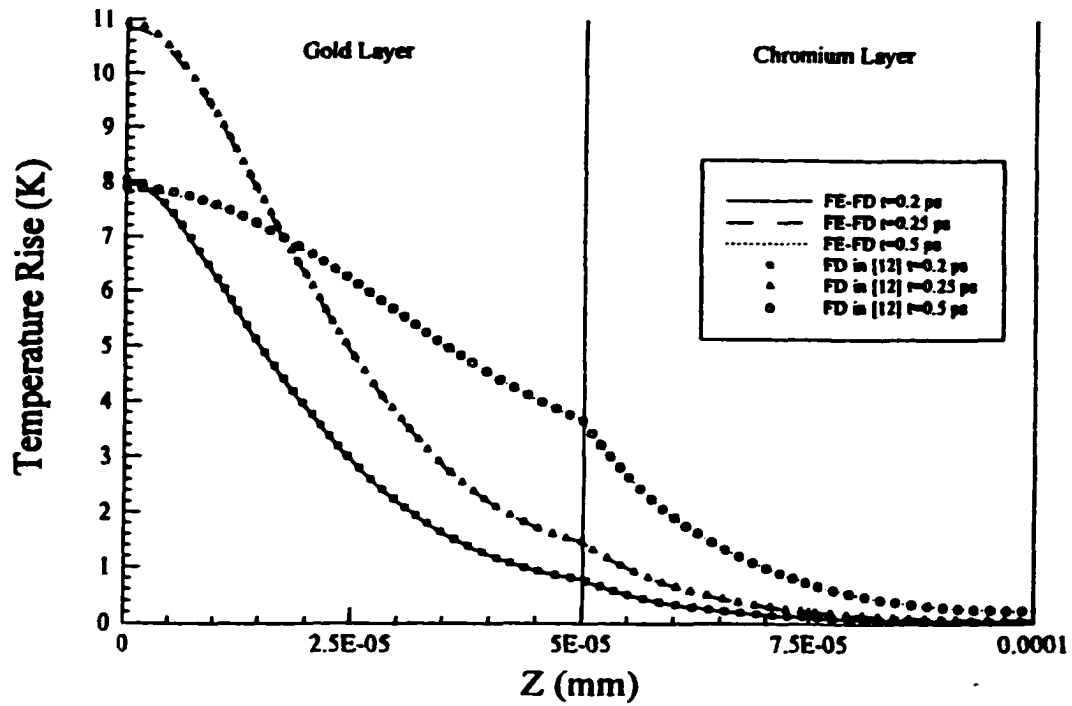


Figure 5.7. Contours of the temperature distribution in the x-z directions ( $t = 0.5$  ps).



**Figure 5.8.** Cylindrical double-layered thin film (heating at the center area).



**Figure 5.9. Temperature profiles along z direction with heat source at center area.**

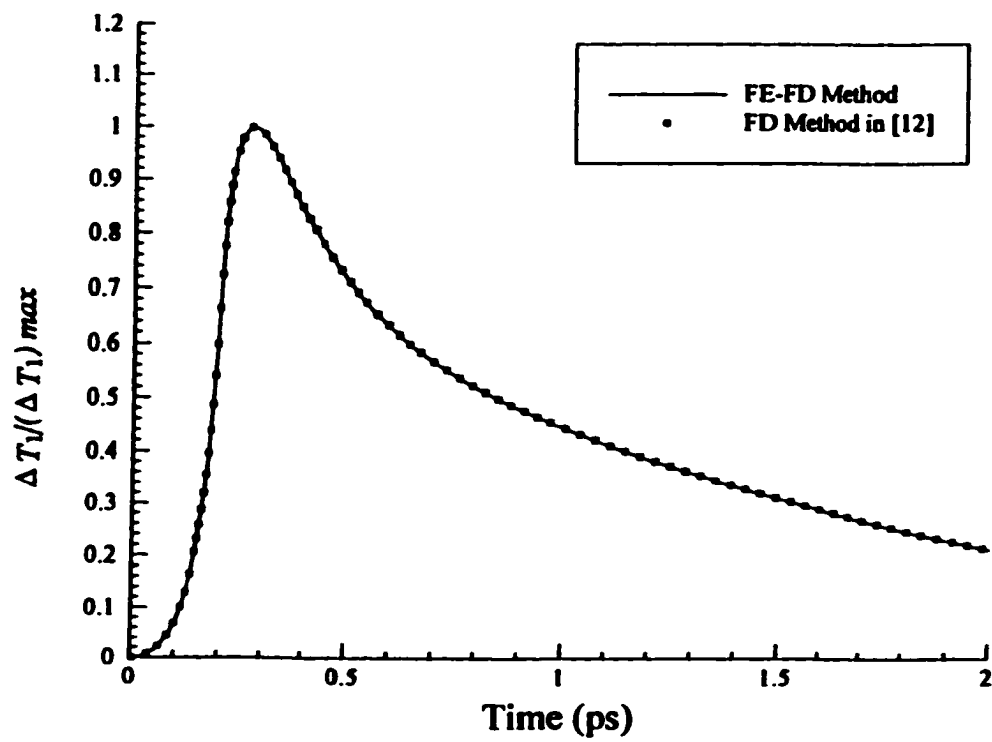


**Figure 5.10.** Temperature change on the center of the surface of the gold layer.

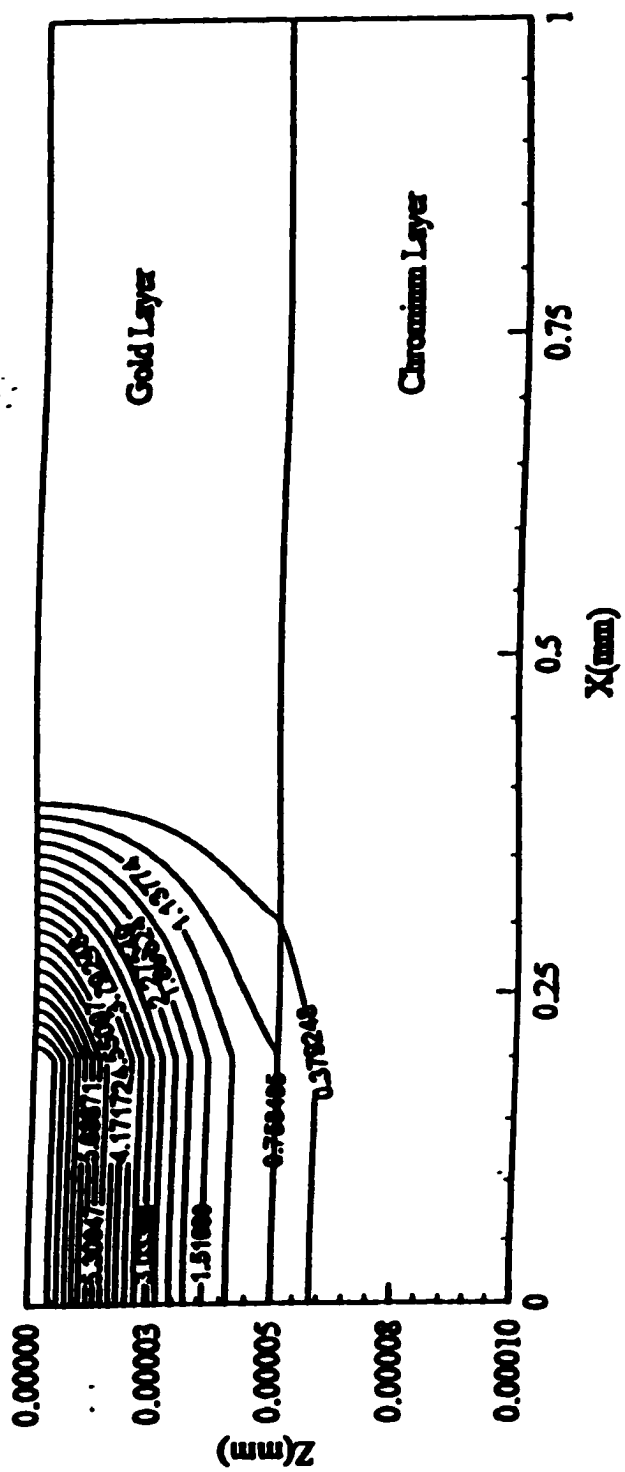


Figure S.11. Contours of the temperature distribution in the x-z direction ( $r=0.2ps$ )

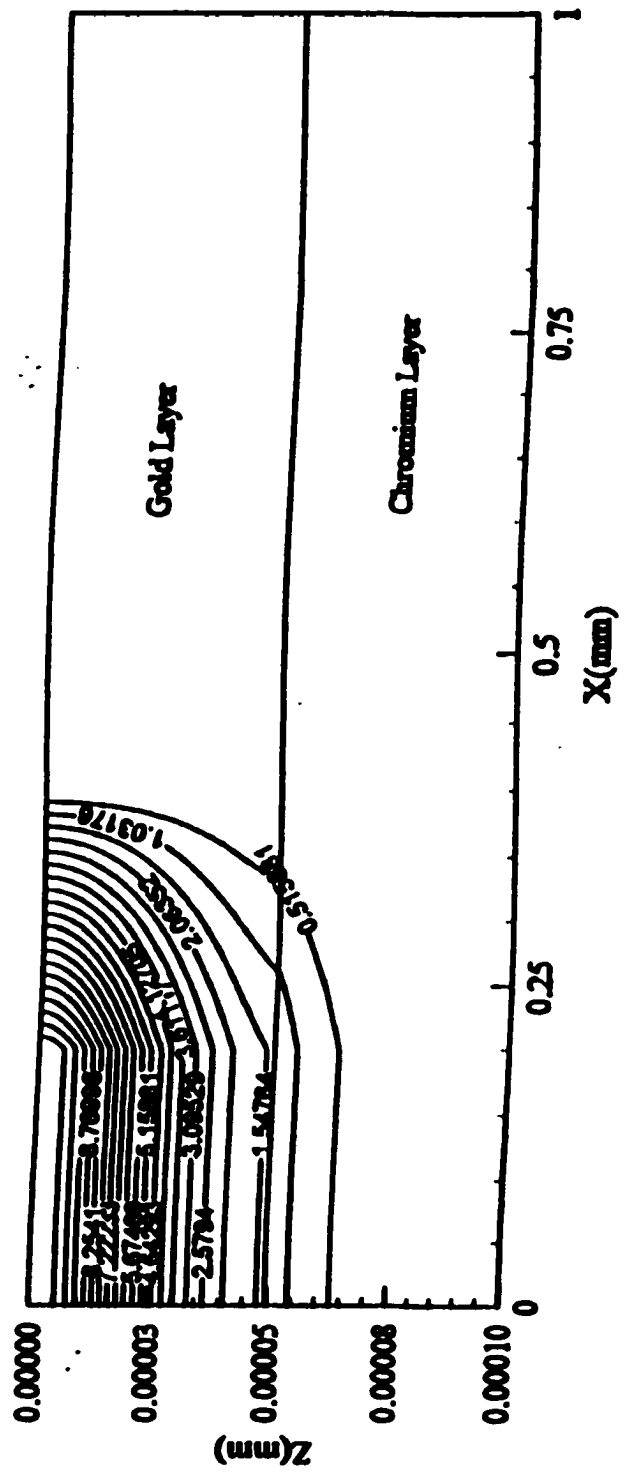


Figure 5.12. Contours of the temperature distribution in the x-z direction ( $t=0.25ps$ )

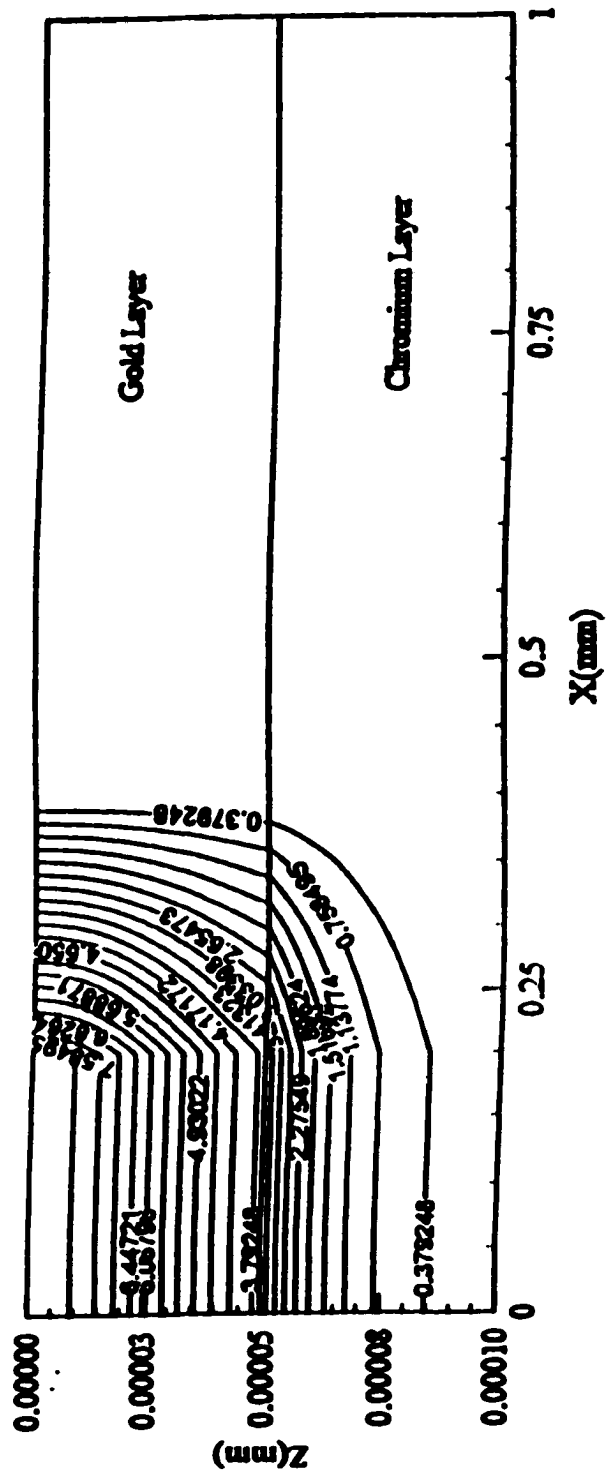


Figure 5.13. Contours of the temperature distribution in the x-z direction ( $t=0.5ps$ )

## **CHAPTER 6**

### **CONCLUSION**

In this dissertation, we have developed a numerical method for solving three-dimensional heat transport equations for a double-layered cylindrical thin film with microscale thickness. The numerical results show that the method is accurate and efficient. Significant results are summarized as follows:

1. The governing equations for thermal analysis of a double-layered cylindrical thin film are set up. The lagging phenomena in the heat transport process has been considered.
2. The governing equations are discretized by using the finite element-finite difference method. To this end, the finite element method is first employed to discretize the equations in the x-y directions. The Crank- Nicholson finite difference method is then applied to the z direction.
3. A domain decomposition for thermal analysis of the double-layered cylindrical thin film has been developed. We first employed a preconditioned Richardson iteration to the discretized scheme so that the equations become two block tri-diagonal linear systems with unknown values at the interface. The parallel Gaussian elimination is then applied to the new system.
4. The temperature rise and temperature distribution in a double-layered thin film are obtained, where a cylindrical gold layer is on a cylindrical chromium

**padding layer.**

- 5. The numerical method can be readily applied to the case that the shape in the x-y directions is arbitrary and the case that the thin film has multilayers. Further, research on distortion for a double-layered thin film caused by thermal expansion is recommended. The governing equations for the stresses, strains, and temperature have been presented in Chapter Three.**

## REFERENCES

- [1] Joseph D. D. and Preziosi L. Heat waves. *Reviews of Modern Physics* 1989. 61:41-73.
- [2] Joshi A. A. and Majumdar A. Transient ballistic and diffusive phonon heat transport in thin films. *Journal of Applied Physics* 1993. 74: 31-39.
- [3] Qiu T. Q. and Tien C. L. Heat transfer mechanisms during short-pulse laser heating of metals. *ASME Journal of Heat Transfer* 1993. 115: 835-841.
- [4] Qiu T. Q. and Tien C. L. Short-pulse laser heating on metals. *International Journal of Heat and Mass Transfer* 1992. 35: 719-726.
- [5] Tzou D. Y. *Macro To Micro Heat Transfer*. Taylor & Francis: Washington, DC., 1996.
- [6] Tzou D. Y. A unified field approach for heat conduction from micro-to macroscales. *ASME Journals of Heat Transfer* 1995. 117: 8-16.
- [7] Tzou D. Y. The generalized lagging response in small-scale and high-rate heating. *International Journal of Heat and Mass Transfer* 1995. 38: 3231-3240.
- [8] Ozisik M. N. and Tzou D. Y. On the wave theory in heat conduction. *ASME Journal of Heat Transfer* 1994. 116: 526-536.
- [9] Tzou D. Y. On the thermal shock wave induced by a moving heat source. *ASME Journal of Heat Transfer* 1989. 111: 232-238.
- [10] Tzou D. Y. Experimental support for the lagging response in heat propagation. *AIAA Journal of Thermophysics and Heat Transfer* 1995. 9: 686-693.
- [11] Chiffell R. J. On the wave behavior and rate effect of thermal and thermomechanical waves. M.S. Thesis, University of New Mexico, Albuquerque, NM, 1994.
- [12] Dai W. and Nassar R. A domain decomposition method for solving three dimensional heat transport equations in a double layered thin film with microscale thickness. Accepted by *Numerical Heat Transfer, Part A*.
- [13] Dai W. and Nassar R. A preconditioned Richardson numerical method for

- [13] Dai W. and Nassar R. A preconditioned Richardson numerical method for thermal analysis in x-ray lithography with cylindrical geometry. *Numerical Heat Transfer, Part A* 1998. 34: 599-616.
- [14] Dai W. and Nassar R. A three dimensional numerical method for thermal analysis in z-ray lithography. *International Journal of Numerical Methods for Heat and Fluid Flow* 1998. 8: 409-423.
- [15] Dai W. and Nassar R. A hybrid finite element-finite difference for thermal analysis in x-ray lithography. *International Journal of Numerical methods for Heat and Fluid Flow* 1999. 9: 660-676.
- [16] Dai W. and Nassar R. A domain decomposition method for solving thin film elliptic interface problems with variable coefficients. *International Journal for Numerical Methods in Engineering* 1999. 45: 747-756.
- [17] Dai W., Nassar R., Warrington R. and Shen B. Three-dimensional numerical model for thermal analysis in r-ray irradiated photoresists. *Numerical Heat Transfer, Part A*, 1997. 31: 585-595.
- [18] Carey G. F. and Oden J. T. *Finite Elements*, Vol. 3. Prentice-Hall: Englewood Cliffs, NJ, 1984.
- [19] Chandrupatla T. R. and Belegundu A. D. *Introduction to Finite Elements in Engineering*. Prentice-Hall: Englewood Cliffs, NJ, 1984.
- [20] Atkinson K. E. *An Introduction to Numerical Analysis* (2nd ed.). Wiley: New York, 1988
- [21] Nering E. D. *Linear Algebra and Matrix Theory*, John Wiley & Sons: New York, 1970.
- [22] Incropera E. P. and Dewitt D. P. *Fundamentals of Heat & Mass Transfer* (3rd ed.). John Wiley & Sons: New York, 1990.